

Cosmological perturbations in the interacting dark sector: Observational constraints and predictions

Joseph P. Johnson,^{1,*} Archana Sangwan,^{1,†} and S. Shankaranarayanan^{1,‡}

¹*Department of Physics, Indian Institute of Technology Bombay, Mumbai 400076, India*

Abstract

We consider an interacting field theory model that describes the interaction between dark energy - dark matter interaction. Only for a specific interaction term, this interacting field theory description has an equivalent interacting fluid description. For inverse power law potentials and linear interaction function, we show that the interacting dark sector model is consistent with *four cosmological data sets* — Hubble parameter measurements (Hz), Baryonic Acoustic Oscillation data (BAO), Supernova Type Ia data (SN), and High redshift HII galaxy measurements (HIIG). More specifically, these data sets prefer a negative value of interaction strength in the dark sector and lead to the best-fit value of Hubble constant $H_0 = 69.9_{1.02}^{0.46}$ km s⁻¹ Mpc⁻¹. Thus, the interacting field theory model *alleviates the Hubble tension* between Planck and these four cosmological probes. Having established that this interacting field theory model is consistent with cosmological observations, we obtain quantifying tools to distinguish between the interacting and non-interacting dark sector scenarios. We focus on the variation of the scalar metric perturbed quantities as a function of redshift related to structure formation, weak gravitational lensing, and the integrated Sachs-Wolfe effect. We show that the difference in the evolution becomes significant for $z < 20$, for all length scales, and the difference peaks at smaller redshift values $z < 5$. We then discuss the implications of our results for the upcoming missions.

* josephpj@iitb.ac.in

† arch06san@gmail.com

‡ shanki@phy.iitb.ac.in

I. INTRODUCTION

Cosmological observations suggest that the energy budget of the Universe is dominated by dark energy and dark matter [1–6]. Λ CDM model provides the simplest description of the Universe dominated by dark energy and dark matter while being highly successful in describing various cosmological observations and phenomena like the cosmic microwave background (CMB) and nucleosynthesis [7]. But with the availability of high precision cosmological observational data, there have been some inconsistencies in the values of cosmological parameters estimated using the Λ CDM model, with the most prominent of them being the difference in the value of the Hubble’s constant estimated from the local distance measurements and CMB observations [8–10]. These inconsistencies point towards the limitations of the Λ CDM model and the need for modifications to the standard model of cosmology.

Apart from the gravitational interaction, we know very little about the properties of dark matter and dark energy. Λ CDM model assumes that dark energy is constant in time. The quintessence model provides a more general time-varying dark energy represented by a scalar field [11, 12]. A quintessence dark energy model can be further generalized by introducing a non-gravitational interaction between dark energy and dark matter, which is not ruled out by cosmological observations [13–38]. Recently, it has been shown that the dark matter-dark energy interaction can reconcile the tensions in the estimated values of Hubble constant H_0 [39–45]. Hence it is important to develop the analytical and numerical tools to detect the interaction between dark energy and dark matter. For this purpose, we need a theoretical framework that provides a comprehensive description of the interacting dark sector.

In Ref.[46], two of the current authors, have explicitly constructed such a framework starting from a classical field theory action which describes interacting dark sector. The authors showed that: (i) A one-to-one mapping between the field theory description and the fluid description of the interacting dark sector exists for a unique interaction term. (ii) This class of interacting dark sector models has an attractor solution describing the accelerated expansion of the Universe. The establishment of such a mapping enables us to analyze the background and perturbed evolution of the Universe with dark energy - dark matter interaction.

To constrain the model parameters, especially the interaction strength, and to make testable predictions, one needs to specify the scalar field potential and the interaction function. In this work, we look at an inverse power law potential [47] $U(\phi) \sim 1/\phi^n$ where ($n = 1, 2$) and a linear interaction function $\alpha(\phi) \sim C\phi$ where $C \in [-1, 1]$. We constrain the cosmological and model parameters using Hubble parameter measurements (Hz) [48–55], high redshift HII Galaxy (HIIG) data [56–61], Baryon acoustic oscillation (BAO) data [62–67] and the Type Ia supernovae (SN) observations [68]. The key results are:

1. Although both negative and positive values of interaction strength (C) are allowed, observations show a preference for negative interaction strength ($C < 0$).
2. For our interacting dark sector model, the constraint on the Hubble constant is $H_0 = 69.9^{+0.46}_{-1.02} \text{ km s}^{-1}\text{Mpc}^{-1}$. Given that the value of Hubble constant reported by Planck is $H_0 = 67.5 \pm 0.5 \text{ km s}^{-1}\text{Mpc}^{-1}$ which uses base Λ CDM cosmology [6] and the distance ladder estimates of Hubble constant is $H_0 = 73.48 \pm 1.66 \text{ km s}^{-1} \text{ Mpc}^{-1}$ (from SH0ES data [69, 70]), and $H_0 = 74.03 \pm 1.42 \text{ km s}^{-1}\text{Mpc}^{-1}$ (measurements of LMC Cepheids [71]), the interacting dark sector model considered in this work alleviate the H_0 tension.
3. The constraints on Ω_m obtained by the model are consistent with $\Omega_m = 0.31 \pm 0.007$ reported in [6] (for latest constraints on the cosmological parameters see [72–80] and the references therein).

Since non-interacting dark energy models and interacting dark energy-dark matter models can explain the current accelerating expansion of the Universe, to distinguish between them, we need to go beyond the background evolution. In this work, we identify three specific tools that we can obtain by studying the difference in the evolution of cosmological perturbations in both of these scenarios [7]: Structure formation, Weak gravitational lensing, and Integrated Sachs-Wolfe effect. More specifically, we look at the evolution of the density perturbation (δ_m), the Bardeen potential, and its derivative (Φ and Φ' respectively) for the inverse power law potential $U(\phi) \sim 1/\phi^n$ where ($n = 1, 2$) and linear interaction function with negative interaction strength ($C < 0$). We evolve all the perturbed quantities in the redshift range $1500 \gtrsim z > 0$. We see a significant difference in the evolution of the relevant perturbed quantities in the interacting and non-interacting scenarios, at all length scales, for $z < 20$ and the maximum difference in the evolution is around $z \sim 5$. We thus explicitly

show that it is possible to detect and constrain the interaction between dark energy and dark matter from cosmological observations.

In Sec. II, we introduce the interacting dark sector model we have used for the analysis. In Sec. III we discuss the background evolution in the model and the numerical analysis using various observational data sets to obtain the parameter constraints. The evolution of the cosmological perturbations and their observational consequences are discussed in Sec. IV. In Sec. V, we briefly discuss the results and discuss the implications of our analysis. Appendices A - C contain additional details.

In this work, we use the natural units where $m_{\text{Pl}}^2 = G$, and the metric signature $(-, +, +, +)$. Greek letters denote the four-dimensional space-time coordinates, and Latin letters denote the three-dimensional spatial coordinates. Unless otherwise specified, *dot* represents derivative with respect to cosmic time and *prime* denotes derivative with respect to number of e-foldings $N \equiv \ln a(t)$.

II. INTERACTING DARK SECTOR: THE MODEL

In this work we consider the model described by the action [46],

$$S = \int d^4x \sqrt{-g} \left(\frac{1}{16\pi G} R - \frac{1}{2} g^{\mu\nu} \nabla_\mu \phi \nabla_\nu \phi - U(\phi) - \frac{1}{2} e^{2\alpha(\phi)} g^{\mu\nu} \nabla_\mu \chi \nabla_\nu \chi - e^{4\alpha(\phi)} V(\chi) \right). \quad (1)$$

where ϕ corresponds to the dark energy and χ corresponds to the dark matter. The dark matter fluid in a homogeneous and isotropic Universe can be described by defining the four velocity u_μ

$$u_\mu = - \left[-g^{\alpha\beta} \nabla_\alpha \chi \nabla_\beta \chi \right]^{-\frac{1}{2}} \nabla_\mu \chi. \quad (2)$$

The energy density (ρ_m) and pressure (p_m) of the dark matter fluid are:

$$p_m = -\frac{1}{2} e^{2\alpha} \left[g^{\mu\nu} \nabla_\mu \chi \nabla_\nu \chi + e^{2\alpha} V(\chi) \right], \quad \rho_m = -\frac{1}{2} e^{2\alpha} \left[g^{\mu\nu} \nabla_\mu \chi \nabla_\nu \chi - e^{2\alpha} V(\chi) \right]. \quad (3)$$

In this description, we can rewrite Einstein's equation in terms of dark energy scalar field and dark matter fluid:

$$G_{\mu\nu} = 16\pi G \left[\nabla_\mu \phi \nabla_\nu \phi - \frac{1}{2} g_{\mu\nu} \nabla^\sigma \phi \nabla_\sigma \phi - g_{\mu\nu} V(\phi) + p_m g_{\mu\nu} + (\rho_m + p_m) u_\mu u_\nu \right], \quad (4)$$

where the energy-momentum tensor for the dark matter fluid is given by

$$T_\nu^{(m)\mu} = p_m g_{\mu\nu} + (\rho_m + p_m) u_\mu u_\nu. \quad (5)$$

The interaction between the dark energy and the dark matter fluid is described by:

$$\nabla_\mu T_\nu^{(m)\mu} = Q_\nu^{(F)}, \quad (6)$$

where the interaction term is given by

$$Q_\nu^{(F)} = -e^{2\alpha(\phi)} \alpha_{,\phi}(\phi) \nabla_\nu \phi [\nabla^\sigma \chi \nabla_\sigma \chi + 4e^{2\alpha(\phi)} V(\chi)] = -\alpha_{,\phi}(\phi) \nabla_\nu \phi (\rho_m - 3p_m). \quad (7)$$

Identifying $T^{(m)} = T_\mu^{(m)\mu} = -(\rho_m - 3p_m)$, we get

$$Q_\nu^{(F)} = T^{(m)} \nabla_\nu \alpha(\phi). \quad (8)$$

The time component of $Q_\nu^{(F)}$ represents the energy transfer between dark energy and dark matter. For easy reading, we denote $Q_0^{(F)}$ as Q . Q will further be split into the background and perturbed parts given by $Q = \bar{Q} + \delta Q$.

To study the cosmological evolution and obtain predictions and constraints, we need to consider a specific form of scalar field potential $U(\phi)$ and the interaction function $\alpha(\phi)$. In this work, we focus on the quintessence dark energy model with an inverse power law potential [47] and a linear interaction function

$$U(\phi) \sim \frac{1}{\phi^n}, \quad \alpha(\phi) \sim \phi, \quad (9)$$

where $n = 1$ and $n = 2$.

III. BACKGROUND EVOLUTION AND OBSERVATIONAL CONSTRAINTS

We consider a spatially flat universe governed by Friedmann equations

$$\left(\frac{\dot{a}}{a}\right)^2 = \frac{8\pi G}{3} \rho_{tot}, \quad \frac{\ddot{a}}{a} = -\frac{4\pi G}{3} (\rho_{tot} + 3P_{tot})$$

where ρ_{tot} and P_{tot} denote the total energy density and pressure of the universe at a given time. At late times, the contribution of the relativistic matter density (ρ_r) is negligible as compared to the dark (non-relativistic) matter (ρ_m) and dark energy density (ρ_ϕ). Hence, in this analysis, we neglect ρ_r and total density is $\rho_{tot} = \rho_m + \rho_\phi$.

The dynamics of the scalar field is governed by

$$(\ddot{\phi} + 3H\dot{\phi} + U_{,\phi})\dot{\phi} = \bar{Q},$$

where, \overline{Q} is the background interaction term. Here, ϕ is in the units of $m_{\text{Pl}} = G^{-1/2}$. The scalar field potential is assumed to be

$$U(\tilde{\phi}) = \kappa m_{\text{Pl}}^2 \tilde{\phi}^{-n}. \quad (10)$$

where κ is of the order of unity. To make the analysis simpler, we rescale the scalar field ϕ to $\tilde{\phi} = \sqrt{16\pi G} \phi$. Note that $\tilde{\phi}$ is dimensionless.

The evolution of non-relativistic matter density is given by

$$\dot{\rho}_m + 3H\rho_m = -\overline{Q},$$

where we have considered a pressureless dark matter fluid, $p_m = 0$. For the interaction term, $\overline{Q} = -\alpha_{,\phi} \dot{\phi} \rho_m$, the above equation gives, $\rho_m = \rho_{m0} e^{-\alpha_{,\phi} \phi} a^{-3}$.

In terms of dimensionless scalar field variable ($\tilde{\phi}$), the Friedmann equations and the field equation are:

$$\left(\frac{\dot{a}}{a}\right)^2 = H_0^2 \Omega_m a^{-3} e^{-C\tilde{\phi}} + \frac{\dot{\tilde{\phi}}^2}{12} + \frac{\kappa m_{\text{Pl}}^2}{12} \tilde{\phi}^{-n} \quad (11)$$

$$\ddot{\tilde{\phi}} + 3H\dot{\tilde{\phi}} + U_{,\tilde{\phi}}(\tilde{\phi}) = -\frac{3H_0^2}{4\pi} C \Omega_m a^{-3} e^{-C\tilde{\phi}}, \quad (12)$$

where we have assumed $\alpha(\tilde{\phi})$ to be a linear function of $\tilde{\phi}$, i. e. $\alpha(\tilde{\phi}) = C\tilde{\phi}$, giving $\alpha_{,\tilde{\phi}} = C$. The parameter C is dimensionless and defines the strength of interaction between dark energy and dark matter. In our analysis, we obtain the constraint on C by keeping it as a free parameter with $C \in [-1, 1]$.

A. Observational data

To constrain the model parameters in the interacting dark sector model, we analyze four different observational data sets. More specifically, we use Hubble parameter measurements (Hz) [48, 49, 51, 54, 81, 82], high redshift HII Galaxy (HIIG) data [56–61], Baryon acoustic oscillation (BAO) data [62–67] and the joint lightcurve analysis (JLA) sample of Type Ia supernovae (SN) observations [68, 83–86].

Hubble Parameter Measurement (H(z)) data: The Hubble parameter measurements (abbreviated as Hz) at different redshifts is an effective tool to constrain the cosmological parameters [48, 51]. Hz observations are useful in constraining the cosmological parameters

as it uses the model parameters directly without having an integral term that might obscure or cover valuable information. Broadly, different techniques employed to measure the Hubble parameters can be classified into two methods: a) Differential age method [81] and b) Radial BAO method [82]. The Hubble rate as a function of redshift is evaluated by using

$$H(z) = -\frac{1}{(1+z)} \frac{dz}{dt}, \quad (13)$$

where t denotes the age of the universe when the observable photon is emitted. In the differential method, we can obtain a direct estimate of expansion rate by taking the derivative of redshift with respect to time. Hubble parameter obtained through this method does not depend on the cosmological model but on the age-redshift relation of cosmic chronometers. So very carefully the selection of passively evolving early galaxies as cosmic chronometers is made depending upon a galaxy's star formation history and its metallicity.

In this work, we consider the Hz data points obtained through the cosmic chronometric technique and use the data points compiled in Ref. [48]. In this compilation, the authors dropped older Hubble parameter estimates from SDSS galaxy clustering [87] and Ly- α forest measurement [88] and added new data sets. Out of the 38 data points reported in Ref. [48], in this analysis, we only use 31 independent measurements of the Hubble parameter ($H(z)$). More specifically, we use 9 data points from Ref. [49], 2 points from Ref. [50], 8 points from Ref. [51], 5 points from Ref. [52], 2 points from Ref. [53], 4 points from Ref. [54], and one point from Ref. [55]. Note that the three points reported in Ref. [89] and another three points in Ref. [62] are also used in the BAO observations, hence removed from this data set.

BAO: Baryon Acoustic Oscillations (BAO) are fluctuations in the correlation function of large scale structure that appears as overdense regions in the distribution of the visible, baryonic matter. This is the consequence of acoustic waves set up in the primordial plasma because of competing forces of radiation pressure and gravity. These acoustic waves travel within the plasma, however are frozen at the time of recombination when the plasma cooled down enough to make the cosmos neutral. The distance where the waves stalls are imprinted as overdense regions and are used as a standard ruler to measure cosmological distances.

The characteristic angular scale of the acoustic peak is given in terms of sound horizon at drag epoch, $r_s(z_d)$, as $\theta_A = r_s(z_d)/D_V(z)$, where, D_V is the effective distance ratio given

in terms of angular diameter distance D_A :

$$D_V(z) = \left[(1+z)^2 D_A(z)^2 \frac{cz}{H(z)} \right]^{1/3}, \quad r_s(z_d) = \int_{z_d}^{\infty} \frac{c_s(z') dz'}{H(z')}. \quad (14)$$

In order to use the BAO data, the knowledge of the sound horizon scale at the z_d (denoted by r_s) is required as the data is given in terms of $H(z) r_s / r_{s, fid}$, $D_M r_{s, fid} / r_s$, $D_V r_{s, fid} / r_s$, where $r_{s, fid}$ is 147.78 Mpc in [62] and [65], and 148.69 Mpc [64] and the comoving angular diameter distance is given by $D_M(z) = (1+z)D_A(z)$. The value of fiducial sound horizon, $r_{s, fid}$ which was calculated by assuming the Λ CDM model and the best fit values of parameters given by Planck-2018 [6], is model dependent, but not to a significant degree. The quantities $D_V r_{s, fid} / r_s$, $D_M r_{s, fid} / r_s$, r_s and $r_{s, fid}$ is given in units of Mpc while $H(z) r_s / r_{s, fid}$ is given in units of $\text{km s}^{-1} \text{Mpc}^{-1}$. We compute r_s is computed using the method given in Ref.[90]. The BAO data in terms of Acoustic parameter $A(z)$ is defined as [91]:

$$A(z) = \left[\frac{100 D_v(z) \sqrt{(\Omega_{NR} h^2)}}{cz} \right]^{1/3}. \quad (15)$$

Thus, the BAO data consists of $A(z)$ and $D_v(z)$ (with associated errors) at different redshifts. The measurement of these distances is a useful tool to constrain cosmological model parameters. The BAO data we use in the analysis lie in the redshift span of $0.106 - 2.36$ and contains 11 points reported in Refs. [62–67].

HIIG: The third data set we use is the high redshift HII galaxy (HIIG) observations [56–61]. These observations are new independent cosmological observations that use the correlation between the Balmer emission line velocity dispersion (σ), and luminosity (L) in HIIG to obtain the distance estimator. This L - σ correlation is given by:

$$\log(L) = \beta \log(\sigma) + \gamma, \quad (16)$$

where, γ and β are the intercept and slope, respectively and $\log = \log_{10}$. The tight correlation between the Balmer line luminosity (L) and velocity dispersion (σ) of the emission lines can be used to constrain the cosmological model parameters.

An extinction correction must be made to the observed fluxes to obtain the values of these parameters. We follow the method used in Ref. [56] and assume the extinction law given in Ref. [92]. The resulting value of the intercept and slope are:

$$\beta = 5.022 \pm 0.058, \quad (17)$$

$$\gamma = 33.268 \pm 0.083, \quad (18)$$

respectively. In our analysis, we use these values of β and γ . Using these values in Eq.(16), we obtain the luminosity of a HII Galaxy. We then use the Luminosity to obtain the distance modulus for that HII Galaxy:

$$\mu_{\text{obs}} = 2.5 \log L - 2.5 \log f - 100.2, \quad (19)$$

where f denotes the measured flux of the HIIG, reported in the HIIG observational data along with error associated with it. We can predict the distance modulus for a given cosmological model by using the theoretical definition:

$$\mu_{\text{th}}(z) = 5 \log D_L(z) + 25, \quad (20)$$

where the luminosity distance $D_L(z)$ (in the units of Mpc) is related to the angular size distance $D_A(z)$ via distance duality relation and the transverse comoving distance $D_M(z)$ through $D_L(z) = (1+z)^2 D_A(z) = (1+z) D_M(z)$. The HIIG data we use comprises 153 measurements that span the redshift range of 0.0088 to 2.429, which covers a larger redshift range than the BAO data used in this analysis.

SN data (JLA): Type Ia supernovae, which are standardizable candles, is another useful tool to determine the expansion history of the Universe [68, 83–86]. The observable reported in the sample is the distance modulus, which is extracted from light curves by assuming that the intrinsic luminosity on average is the same for Type Ia supernovae with the identical color, shape, and environment, irrespective of the redshift measurement. The standardized distance modulus, obtained by using the following linear empirical relation:

$$\mu^{\text{obs}} = m_B^* + \alpha x_1 - \beta C - M_B. \quad (21)$$

Here, m_B^* is the peak magnitude observed in the B-band rest frame, α and β are nuisance parameters, C is the color of supernovae at peak brightness, and x_1 is ‘stretch’ of the light curve. The values of the parameters (m_B, x_1, C) are obtained by fitting supernovae spectral sequence to the photometric data. The parameter M_B , which is the absolute B-band magnitude, depends on the host stellar mass. Theoretical value of the distance modulus μ_{th} is given by Eq. (20), which depends on the cosmological model.

By measuring the apparent brightness and comparing it to other candles, one can estimate the distance the photons have traveled, and hence the rate of expansion of the Universe. Our analysis uses the full joint lightcurve analysis (JLA) sample comprising 740 type Ia

Supernovae spanning a redshift range of $z=0.01$ to $z=1.4$. We use the abbreviation ‘SN’ to denote these 740 sample points.

B. Data analysis technique

For our analysis, we use the χ^2 minimization technique. Any measurement data contains an observable quantity $X_o(z_i)$ and its corresponding redshift z_i , along with the error associated with each point σ_i . Here, ‘ i ’ takes the values upto N (number of data points in each observation). We can also estimate these observable quantities theoretically $[X_{th}(z_i)]$ for the models considered in the analysis.

For $H(z)$ data, the observable is the expansion rate and we consider 31 points obtained using cosmic chronometer and the χ^2 is defined as:

$$\chi_H^2(\mathbf{p}) = \sum_{i=1}^{31} \frac{[H_{th}(\mathbf{p}, z_i) - H_o(z_i)]^2}{\sigma_i^2}, \quad (22)$$

where, σ_i is the uncertainty of $H_o(z_i)$. All these 31 points are independent of each other and expansion rate depend on the specific model chosen represented by ‘ \mathbf{p} ’ in the above expression.

The BAO data is a correlated data, so to calculate the χ^2 , we need to use the covariance matrix in the definition, i. e.,

$$\chi_{BAO}^2(\mathbf{p}) = [X_{th}(\mathbf{p}) - X_o(z_i)]^T \mathbf{C}^{-1} [X_{th}(\mathbf{p}) - X_o(z_i)], \quad (23)$$

where superscripts T and -1 denote the transpose and inverse of the matrices, respectively. For the data, we use the covariance matrix \mathbf{C} from Ref. [62].

For HIIIG data consisting of 153 measurements, the χ^2 is given by

$$\chi_{HIIIG}^2(\mathbf{p}) = \sum_{i=1}^{153} \frac{[\mu_{th}(\mathbf{p}, z_i) - \mu_o(z_i)]^2}{\sigma_i'^2}, \quad (24)$$

where σ_i' is the uncertainty of the i_{th} measurement (not to be confused with the velocity dispersion (σ) term in HIIIG measurements) and is given by

$$\sigma' = \sqrt{\sigma_{stat}^{\prime 2} + \sigma_{sys}^{\prime 2}}. \quad (25)$$

σ'_{stat} is the statistical uncertainties and is given by:

$$\sigma_{stat}^{\prime 2} = 6.25 [\sigma_{\log f}^{\prime 2} + \beta^2 \sigma_{\log \sigma}^{\prime 2} + \sigma_{\beta}^{\prime 2} (\log \sigma)^2 + \sigma_{\gamma}^{\prime 2}] + \left(\frac{\partial \mu_{th}}{\partial z} \right)^2 \sigma_z^{\prime 2}. \quad (26)$$

Due to the distance modulus term in the expression, the systematic uncertainty calculated this way is model-dependent. However, when it comes to constraining the cosmological parameters, the model dependence is negligible [93]. In this analysis, we do not account for systematic uncertainties similar to the earlier work [56, 93] and take the statistical uncertainty as total uncertainty, i. e., $\sigma = \sigma_{\text{stat}}$.

For the SN data with 740 joint light curves sample, the χ^2 function is:

$$\chi_{\text{SN}}^2(\mathbf{p}) = \sum_{i=1}^{740} \frac{[\mu_{\text{th}}(\mathbf{p}, z_i) - \mu_{\text{o}}(z_i)]^2}{\sigma_i^2}, \quad (27)$$

with σ_i giving the total uncertainty of the i_{th} measurement.

For the joint analysis (Hz+BAO+HIIG+SN), we obtain the joint likelihood ($e^{-\chi^2}$) by multiplying individual likelihoods such that $\chi^2 = \chi_H^2 + \chi_{\text{BAO}}^2 + \chi_{\text{HIIG}}^2 + \chi_{\text{SN}}^2$. Here, the maximum likelihood corresponds to the minimum value of χ^2 .

C. Parameter constraints

Having discussed the data sets and the technique, we can now obtain parameter constraints for the interacting dark sector model discussed at the starting of this section. More specifically, we use the χ^2 technique (described in Sec. III B) to obtain the 1σ , 2σ , and 3σ confidence regions corresponding to the four data sets for various cosmological parameters used in our dark energy- dark matter interaction model. For a given value of n in the scalar-field potential (10), we obtain the constraints on the standard model parameters H_0 , Ω_m , w_0 and the parameter C , which describes the interaction strength in the dark sector.

For the parameter fitting, we use priors that are consistent with the different constraints obtained from various observations. For the Hubble constant, we take the range to be $H_0 = 60 - 80 \text{ km s}^{-1} \text{ Mpc}^{-1}$. The present-day value of the dark-energy equation of state parameter is set to be between $-1 \leq w_0 \leq 1$. The non-relativistic matter density is taken to be in the range $0.01 \leq \Omega_m \leq 0.6$, and the interaction strength between dark matter-dark energy is taken to be between $-1 \leq C \leq 1$. These priors are listed in Table I.

Parameter	Lower Limit	Upper Limit
H_0	60.0	80.0
Ω_m	0.1	0.6
w_0	-1.0	1.0
C	-1.0	1.0

TABLE I: Priors used in the analysis of parameter fitting.

Figure 1 contains the constraints on parameters H_0 , interaction strength C , and Ω_m for the four observational data sets. The plots are for $n = 1$ (10). Analysis is also done for $n = 2$ and $n = 3$; however, there is no significant change in the parameter constraints. For completeness, in Appendix A, we have presented the results for $n = 2$. The 1σ , 2σ , 3σ contours corresponding to 67%, 95% and 99% confidence regions respectively, are shown in two-dimensional planes in Figure 1. The first, second, and third columns correspond to ‘ $H_0 - \Omega_m$ ’, ‘ $H_0 - C$ ’ and ‘ $\Omega_m - C$ ’ planes, respectively. To show these two-dimensional confidence regions, we have marginalized over the other parameters. The two-dimensional confidence regions for standard parameters w_0 and Ω_m are shown in Figure 2. Table II contains the best fit values of the parameters, and Table III contains the allowed range of parameters. In the first row, we show constraints from Hz measurements. In the second row, results from BAO+Hz observations are shown, and the third row represents the confidence contours from HIIG data, while results in the fourth row are from SN+Hz observations. The fifth row shows the constraints obtained from the combination of all the data sets mentioned in section III A.

Observations	H_0	Ω_m	C	w_0	χ^2_{min}
Hz	69.34	0.29	0.98	-0.989	18.81
BAO+Hz	70.67	0.3	-0.63	-0.992	22.43
HIIG	71.3	0.29	-0.52	-0.98	410.12
SN+Hz	69.51	0.31	-0.69	-1.0	737.21
All combined	69.9	0.29	-0.47	-0.99	1152.3

TABLE II: The best fit values of the parameters obtained for the dark-energy dark-matter interaction model.

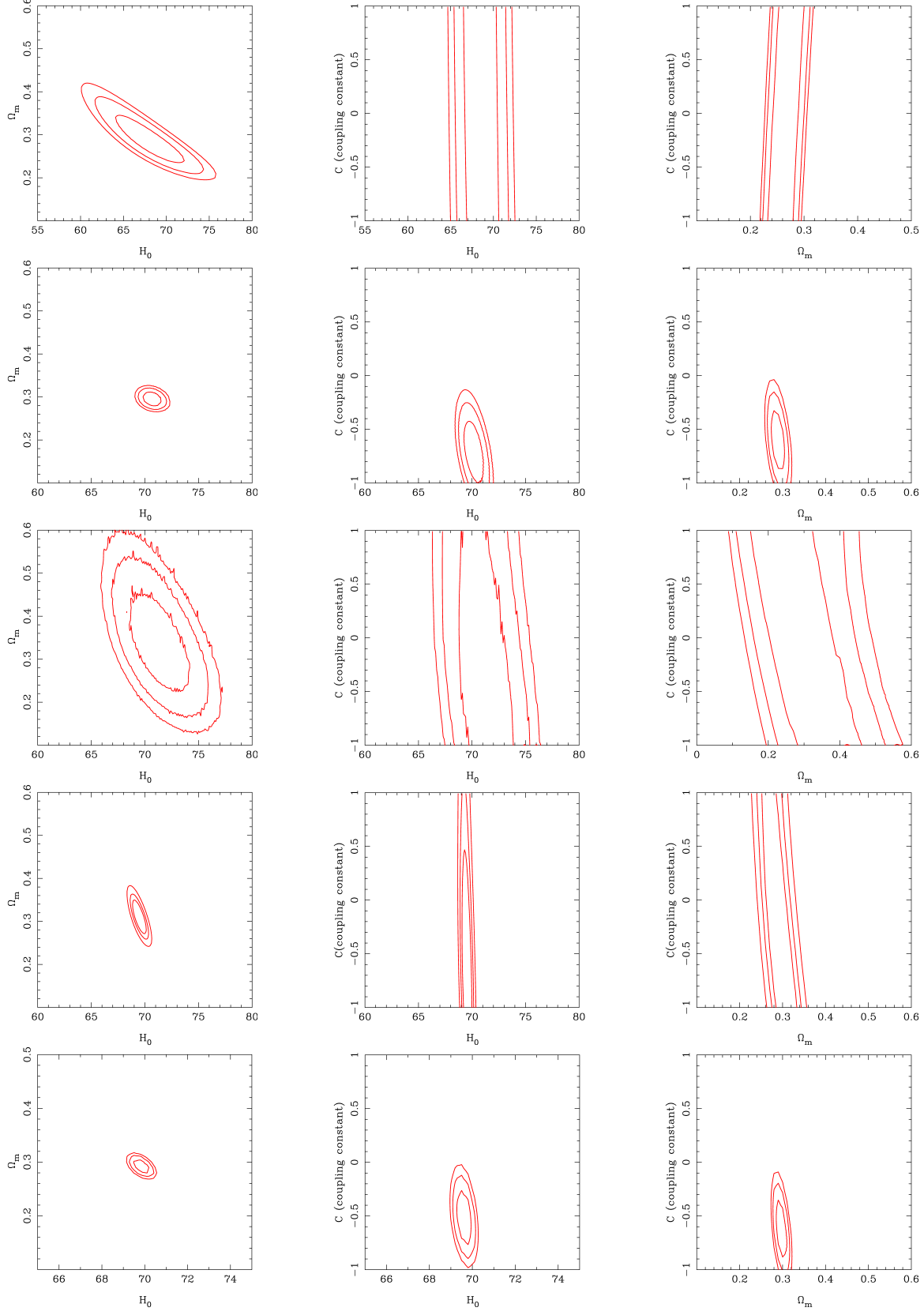


FIG. 1: 1,2,3- σ likelihood contours for Hz data (I row), BAO+Hz data (II row), HIIG data (III row), SN+Hz data (IV row) and all four data sets (V row). The two-dimensional contours are obtained by performing marginalization over other parameters. 13

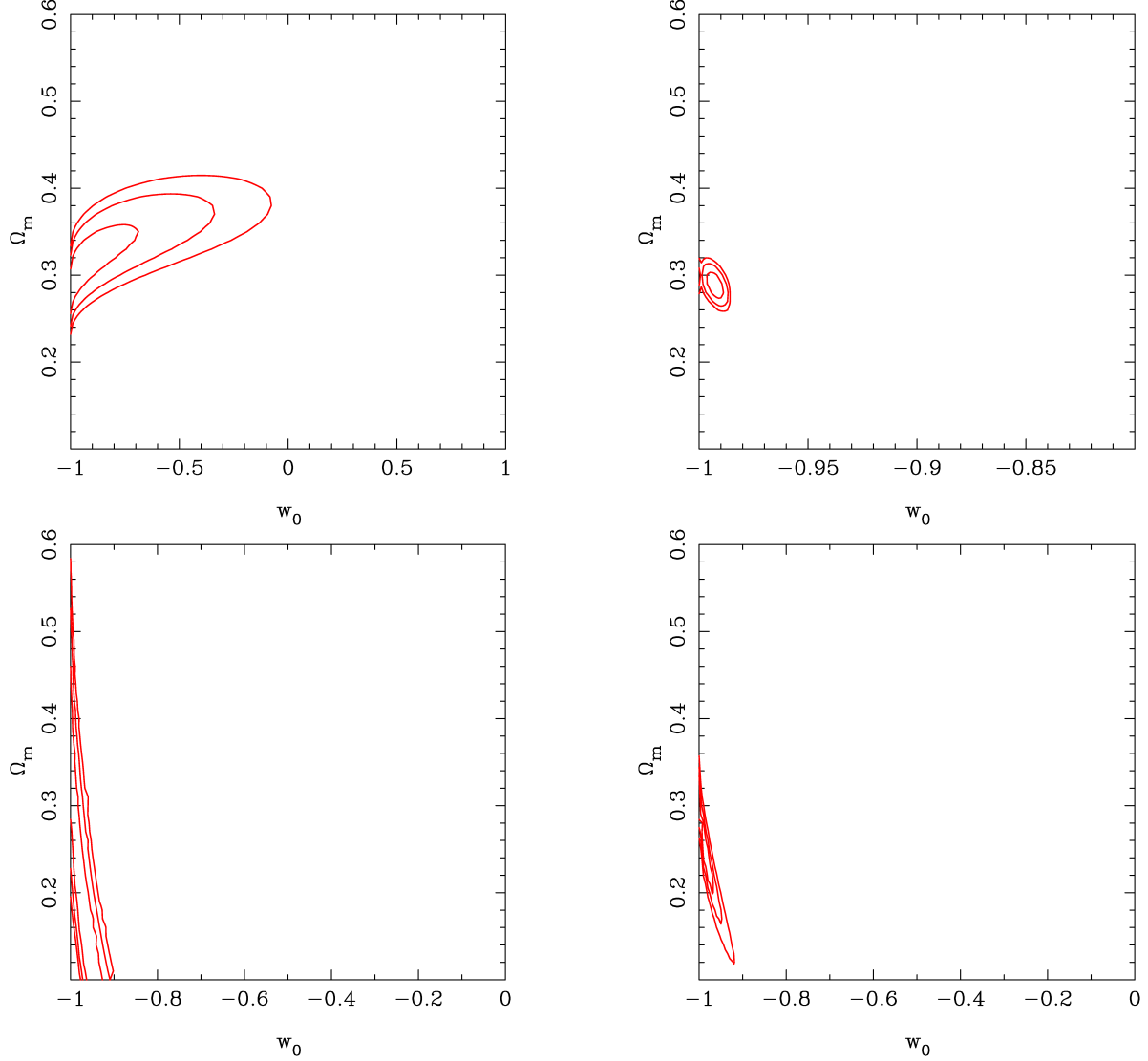


FIG. 2: 1,2,3- σ likelihood contours in ' w_0 - Ω_m ' plane. The top row shows constraints from Hz data (left) and BAO+Hz observations (right). The second row shows constraints from HIIG measurements (left) and SN+Hz observations (right).

The key inferences from the Hz data are as follows: First, the minimum value of χ^2 is 18.81 which corresponds to the best fit values of the parameters $H_0 = 69.34 \text{ km s}^{-1} \text{ Mpc}^{-1}$, $\Omega_m = 0.29$, $w_0 = -0.98$ and the interaction strength $C = 0.98$. Second, within the 2σ region, the Hz data allows H_0 to take values between $61.19 - 74.12 \text{ km s}^{-1} \text{ Mpc}^{-1}$ which includes the values reported by Planck [6] and the local measurements [70, 94]. Hence, with Hz observations, the interacting dark sector model is consistent with both of these reported values. Third, the best fit value, as well as the allowed range of non-relativistic density parameter, is also

Data set	1σ Confidence	2σ confidence	3σ confidence
Hz	$64.19 \leq H_0 \leq 72.11$ $0.24 \leq \Omega_m \leq 0.34$ $-1 \leq w_0 \leq -0.67$ $-1 \leq C \leq 1$	$61.19 \leq H_0 \leq 74.12$ $0.21 \leq \Omega_m \leq 0.39$ $-1 \leq w_0 \leq -0.24$ $-1 \leq C \leq 1$	$59.76 \leq H_0 \leq 75.91$ $0.19 \leq \Omega_m \leq 0.43$ $-1 \leq w_0 \leq 0.04$ $-1 \leq C \leq 1$
BAO+Hz	$69.42 \leq H_0 \leq 71.16$ $0.28 \leq \Omega_m \leq 0.31$ $-0.997 \leq w_0 \leq -0.988$ $-0.87 \leq C \leq -0.29$	$69.07 \leq H_0 \leq 71.86$ $0.28 \leq \Omega_m \leq 0.32$ $-0.999 \leq w_0 \leq -0.983$ $-1 \leq C \leq -0.12$	$68.73 \leq H_0 \leq 72.11$ $0.27 \leq \Omega_m \leq 0.33$ $-1 \leq w_0 \leq -0.98$ $-1 \leq C \leq 0.01$
HIIG	$68.88 \leq H_0 \leq 74.98$ $0.22 \leq \Omega_m \leq 0.43$ $-1 \leq w_0 \leq -0.92$ $-1 \leq C \leq 1$	$67.82 \leq H_0 \leq 75.43$ $0.16 \leq \Omega_m \leq 0.53$ $-1 \leq w_0 \leq -0.9$ $-1 \leq C \leq 1$	$66.98 \leq H_0 \leq 76.31$ $0.13 \leq \Omega_m \leq 0.6$ $-1 \leq w_0 \leq -0.89$ $-1 \leq C \leq 1$
SN+Hz	$69.18 \leq H_0 \leq 70.02$ $0.25 \leq \Omega_m \leq 0.33$ $-1 \leq w_0 \leq -0.97$ $-1 \leq C \leq -0.51$	$69.06 \leq H_0 \leq 70.19$ $0.24 \leq \Omega_m \leq 0.34$ $-1 \leq w_0 \leq -0.93$ $-1 \leq C \leq 1$	$68.87 \leq H_0 \leq 70.36$ $0.22 \leq \Omega_m \leq 0.35$ $-1 \leq w_0 \leq -0.9$ $-1 \leq C \leq 1$
Hz+BAO+HIIG+SN	$69.35 \leq H_0 \leq 70.04$ $0.28 \leq \Omega_m \leq 0.31$ $-0.997 \leq w_0 \leq -0.988$ $-0.68 \leq C \leq -0.26$	$69.01 \leq H_0 \leq 70.23$ $0.27 \leq \Omega_m \leq 0.32$ $-0.998 \leq w_0 \leq -0.985$ $-1 \leq C \leq -0.96$	$68.88 \leq H_0 \leq 70.36$ $0.26 \leq \Omega_m \leq 0.33$ $-0.999 \leq w_0 \leq -0.983$ $-1 \leq C \leq 0.05$

TABLE III: Confidence limits from various data sets for interacting dark sector cosmology.

consistent with the constraints reported in the previous studies [6, 70, 94]. Fourth, after marginalizing over parameter w_0 , the data allows the entire range of the coupling parameter (C) considered in the analysis within the 1σ region see Figure 1. However, we also find that if we fix w_0 at a particular value, say $w_0 = -1$, it does not constrain C at all, but if we move away from Λ CDM like scenarios at present, and consider $w_0 \geq -1$ then we start getting a limit on C as well. As the value of w_0 moves away from -1 towards 1, the constraints on C becomes tighter (cf. Figure 3). Fifth, from Figure 2, we see that the Hz data does not

provide a lower limit on w_0 ; however, an upper limit of -0.67 within 1σ and $w_0=0.04$ within 3σ region is allowed showing that this particular model does not allow for a non-accelerating universe within 1σ region. Also, Hz is the only observation that allows for a non-accelerating universe within the 3σ region. The allowed range for w_0 is the widest compared to the other three observations considered in the analysis. The Hz measurements constrain Ω_m to take values within a range of $0.19 - 0.43$ for 3σ confidence level, which is very wide compared to the ones obtained from BAO+Hz and SN+Hz data sets.

The key inferences from BAO+Hz data are as follows: First, the minimum value of χ^2 is 22.43 which corresponds to the best fit values of parameters giving $H_0 = 70.67 \text{ km s}^{-1}\text{Mpc}^{-1}$, $\Omega_m = 0.3$, $w_0 = -0.992$ and the interaction strength is $C = -0.63$. Second, within 1σ region, BAO+Hz data allows H_0 to take a very small range given by $69.4 - 71.1 \text{ km s}^{-1}\text{Mpc}^{-1}$ which lies between the value of H_0 reported by Planck [6] and the local probes [70, 94]. *Therefore, the interacting dark sector model can alleviate the H_0 tension.* Third, the best fit value of the non-relativistic matter density parameter is $\Omega_m = 0.3$. The allowed range within the 3σ region is very narrow and consistent with the constraints reported in the previous studies [6, 70, 94]. Fourth, within 1σ , BAO+Hz data also constrains the interaction strength C within the range of -0.87 to -0.29 (cf. Figure 1) and between -1 to 0.01 corresponding to 99% confidence region. *Thus, BAO+Hz data prefers negative values of C .* Here again, we find that if we fix w_0 at a particular value, say $w_0 = -1$, the allowed range is narrower than when w_0 was a free parameter. And if we move away from Λ CDM like scenarios at present, and consider $w_0 \geq -1$ then the upper limit on C starts getting lower as the contours start shifting to the negative regions on C . As we change w_0 from -1 towards 1 , the constraints on C becomes tighter as in Hz data, and we find that the BAO+Hz data prefers negative values of C .

Fifth, from Figure 2, we see that the BAO+Hz data provide very small range on w_0 for 1σ , 2σ region and within 3σ region Λ CDM case is allowed. Therefore, the BAO+Hz observational data *do not* allow for a non-accelerating universe and prefer a Λ CDM like scenario. It also provides the tightest constraints for the model parameters out of all the observations considered.

The key inferences from HIIG data are as follows: First, the minimum value of χ^2 is 410.12 which corresponds to the best fit parameters $H_0 = 71.3 \text{ km s}^{-1}\text{Mpc}^{-1}$, $\Omega_m = 0.29$, $w_0 = -0.98$ and the interaction strength is $C = -0.52$. Second, HIIG data allows H_0 to

take values in the range $68.88 - 74.98 \text{ km s}^{-1}\text{Mpc}^{-1}$ within 1σ region. The best fit value for the model indicates the preference for the value of H_0 reported by local measurements [70, 94]. However, the interacting dark sector model is also consistent with the H_0 value reported in Ref. [6] within 3σ region. Third, the best fit value, as well as the allowed range of non-relativistic density parameter, is also consistent with the constraints reported in the previous studies [6, 70, 94]. Fourth, similar to Hz data, HIIG data allows the entire range of coupling parameter (C) within 1σ region, see Figure 1. Here again, we have marginalized over parameter w_0 . We also found that if we fix w_0 at a particular value and consider $w_0 \geq -1$, then we start getting a limit on C as well. As the value of w_0 moves away from -1 towards 1 , the constraints on C becomes tighter.

Fifth, from Figure 2, we see that the HIIG data does not provide a lower limit on w_0 . Still, an upper limit of -0.9 within the 3σ region is allowed, showing that similar to BAO+Hz data, this particular model does not allow for a non-accelerating universe within 3σ region. The results are consistent with the Λ CDM model. The constraints on Ω_m by these observations give the widest range amongst all data sets considered in the analysis.

The key inferences from SN+Hz data are as follows: First, the minimum value of χ^2 is 737.21 which corresponds to the best fit values of the parameters $H_0 = 69.51 \text{ km s}^{-1}\text{Mpc}^{-1}$, $\Omega_m = 0.31$, $w_0 = -1.0$ and $C = -1$. Second, the SN+Hz data allows H_0 to take values between $\sim 69.18 - 70.02 \text{ km s}^{-1}\text{Mpc}^{-1}$ within 1σ region, which lies between the values reported by Planck-2018 [6] and the local H_0 measurements [70, 94]. Interestingly, it provides a very narrow range for H_0 and, hence, *the interacting dark sector model helps alleviate the H_0 tension*. Third, the best fit value, as well as the allowed range of non-relativistic density parameter, is also consistent with the constraints reported in previous studies [6]. Fourth, like Hz data, SN+Hz data also allows the entire range of the interaction strength (C) within the 3σ region. However, within 1σ region, it constrains C to be less than 0.5 , (cf. Figure 1). Here again, we have marginalized over parameter w_0 . We find that, like other data sets, SN+Hz also prefers negative values of interaction strength.

Fifth, from Figure 2, we see that the SN+Hz data does not provide a lower limit on w_0 . However, within the 1σ , there is an upper limit of -0.97 , and $w_0 = -0.9$ within the 3σ region. Thus, the analysis shows that a non-accelerating universe is not allowed. The allowed values of Ω_m are very narrow and consistent with previous studies. This model is also consistent with the Λ CDM model.

The key inferences from the combined data are as follows: First, the minimum value of χ^2 is 1152.3, which corresponds to the best fit values of the parameters are $H_0 = 69.9$ km s⁻¹Mpc⁻¹, $\Omega_m = 0.29$, $w_0 = -0.99$ and the interaction strength is $C = -0.47$. Second, the Hz+BAO+HIIG+SN data allows H_0 to take values between $\sim 69.35 - 70.04$ km s⁻¹Mpc⁻¹ within 1σ region, which lies between the values reported by Planck-2018 [6] and the local probes [70, 94]. It provides a very narrow range for H_0 within the 3σ confidence region. Therefore, this dark sector interaction model puts very narrow constraints on model parameters to alleviate the H_0 tension with the joint analysis. Third, the best fit value, as well as the allowed range of non-relativistic density parameter, is also consistent with a narrow range of allowed values with $0.33 \geq \Omega_m \geq 0.26$ within 3σ region, and these constraints are consistent with the ones reported in previous studies [6, 70]. Fourth, we get a very narrow range for the coupling parameter for the joint analysis, C , which restricts it to take values only within -0.68 to -0.26 for 1σ and from -1 to 0.05 for 3σ confidence regions, see Figure 1. In the joint analysis, the constraints are driven by the BAO observation, which has the most constraining capacity, followed by SN, Hz, and HIIG observations. Similar to the individual cases, if we fix w_0 at a particular value, say $w_0 = -1$, the combination data gives slightly narrower range, but if we move away from Λ CDM like scenarios at present. For $w_0 \geq -1$, there is a preference for negative values of C .

Fifth, from Figure 2, we see that the combined data does not provide a lower limit on w_0 . However, within 1σ , we get the upper limit of -0.993 and $w_0 = -0.99$ within 3σ region. This again shows that the model does not allow for a non-accelerating universe and constrains w_0 to a value close to -1, and is consistent with the Λ CDM model.

In Figure 3, instead of marginalizing w_0 , we assume a value of w_0 within 3σ allowed range reported in this work and see the change in the $H_0 - C$ plane. The first row is obtained for Hz data, and the value of w_0 considered are -1, -0.6, and -0.1 (left, middle, and right plots, respectively). In the second, third, fourth, and fifth rows, the results correspond to BAO+Hz, HIIG, SN+Hz, and combined analysis, respectively. For the left, middle and right plots respectively, we fix w_0 at -1, -0.997 and -0.995. For Hz measurements, we see a significant change in the constraints as w_0 changes from -1 to -0.1 , and we start getting constraints on C . But for BAO+Hz, HIIG, SN+Hz, and combined case, there is a slight shift in contours in contours when w_0 is varied from $w_0 = -1$ to -0.995 (within 3σ range).

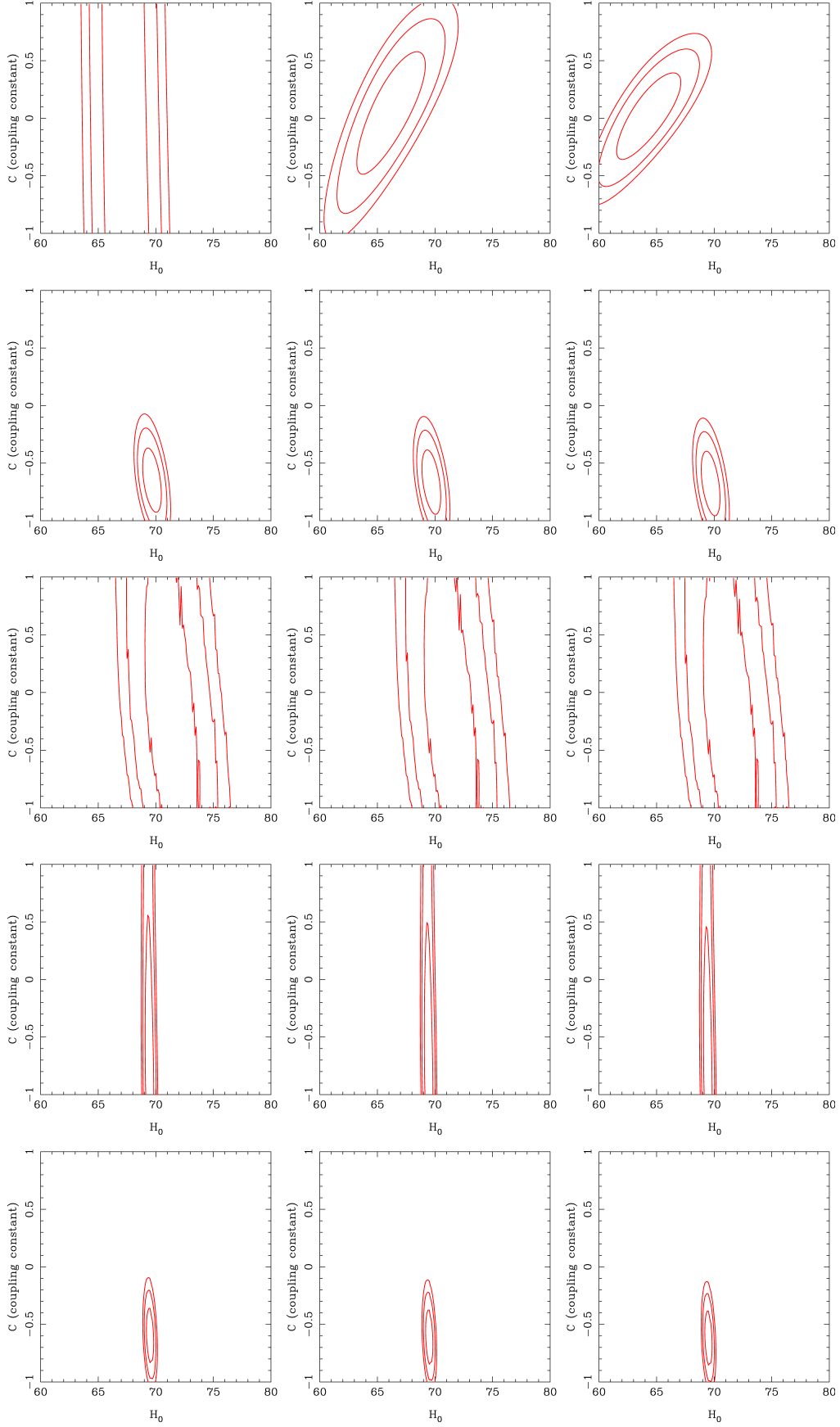


FIG. 3: 1,2,3- σ likelihood contours in ' H_0-C ' plane for different values of w_0 . The top row shows constraints from Hz data (I row), BAO+Hz (II row), HIIG data (III row), SN+Hz (IV row) and all four data sets (V row). The left, middle and right plots correspond to different values of w_0 .

Thus, from these analyses we make the following conclusions:

1. The model helps to alleviate the H_0 tension. All the observational data sets considered constrain H_0 to be close to $70 \text{ km s}^{-1}\text{Mpc}^{-1}$.
2. The constraints on Ω_m obtained from various data sets are consistent with each other.
3. The constraints on w_0 are consistent with Λ CDM model, and only Hz data allows for a non-accelerating universe.
4. All data sets, except Hz, prefer negative value for the interaction strength (C).
5. We have analyzed for $n = 2$ and the parameter constraints are roughly the same. (See Appendix A.)

IV. EVOLUTION OF THE SCALAR PERTURBATIONS AND PREDICTIONS OF THE MODEL

In the previous sections, we have obtained the constraints on the various model parameters based on the observational data related to the background evolution of the Universe. In this section, we look at the evolution of first-order perturbations for negative value for the interaction strength (C).

The perturbed FRW metric in the Newtonian gauge given by [7]:

$$g_{00} = -(1 + 2\Phi), \quad g_{0i} = 0, \quad g_{ij} = a^2(1 - 2\Psi)\delta_{ij}, \quad (28)$$

where $\Phi \equiv \Phi(t, x, y, z)$ and $\Psi \equiv \Psi(t, x, y, z)$ are the Bardeen Potentials.

We obtain the evolution of three perturbed quantities, which are relevant to three different cosmological observations:

1. Structure formation: $\delta_m(t, x, y, z) \equiv \frac{\delta\rho_m(t, x, y, z)}{\bar{\rho}_m(t)}$
2. Weak lensing : $\Phi + \Psi$
3. Integrated Sachs-Wolfe (ISW) effect: $\Phi' + \Psi'$

where δ_m is the density perturbation of dark matter fluid. We study the evolution of these perturbed quantities for various length scales specified by the wavenumber k .

To analyze the difference in the evolution of the scalar perturbations in dark sector interactions compared to standard cosmology, we study the following quantities:

$$\Delta\delta_m = \delta_{m_i} - \delta_{m_{ni}}, \quad \Delta\delta_{m_{rel}} = \frac{\delta_{m_i} - \delta_{m_{ni}}}{\delta_{m_{ni}}} = \frac{\Delta\delta_m}{\delta_{m_{ni}}} \quad (29a)$$

$$\Delta\Phi = \Phi_i - \Phi_{ni}, \quad \Delta\Phi_{rel} = \frac{\Phi_i - \Phi_{ni}}{\Phi_{ni}} = \frac{\Delta\Phi}{\Phi_{ni}} \quad (29b)$$

$$\Delta\Phi' = \Phi'_i - \Phi'_{ni}, \quad \Delta\Phi'_{rel} = \frac{\Phi'_i - \Phi'_{ni}}{\Phi'_{ni}} = \frac{\Delta\Phi'}{\Phi'_{ni}} \quad (29c)$$

where the subscripts i and ni denote the interacting and non-interacting scenarios, respectively.

The perturbed interaction term in the fluid description is given by

$$\delta Q^{(F)} = -(\delta\rho_m - 3\delta p_m)\alpha_{,\phi}(\bar{\phi})\dot{\bar{\phi}} - (\bar{\rho}_m - 3\bar{p}_m) \left[\alpha_{,\phi\phi}(\bar{\phi})\dot{\bar{\phi}}\delta\phi + \alpha_{,\phi}(\bar{\phi})\dot{\delta\phi} \right] \quad (30)$$

We use the evolution equations and dimensionless variables introduced in Ref. [46] to obtain the evolution of the scalar perturbations. In the dimensionless variables, the evolution equations are:

$$\begin{aligned} & \delta\phi'' + \left[\frac{3}{2}(y^2 - x^2 - \omega\Omega_m + 1) - 3\sqrt{6}\alpha\beta x \left(c_s^2 - \frac{1}{3} \right) \right] \delta\phi' \\ & + \left[-9\beta \left(\Omega_m\gamma \left(\omega - \frac{1}{3} \right) \beta - y^2 \left(c_s^2 - \frac{1}{3} \right) \lambda \right) \alpha + 3\Gamma\lambda^2 y^2 + \frac{k^2}{a^2 H^2} \right] \delta\phi \\ & + \left[-18\sqrt{2}\alpha\beta \left(c_s^2 - \frac{1}{3} \right) - 8\sqrt{3}x \right] \Phi' \\ & - 18\sqrt{2} \left[\alpha\beta \left(\left(c_s^2 - \frac{1}{3} \right) \left(y^2 + \frac{k^2}{3a^2 H^2} \right) + (c_s^2 - \omega) \right) + \frac{\lambda y^2}{3} \right] \Phi = 0 \quad (31) \end{aligned}$$

$$\begin{aligned} & \Phi'' + \frac{3}{2} \left[y^2 - x^2 - \Omega_m\omega + 2c_s^2 + \frac{5}{3} \right] \Phi' + 3 \left[c_s^2 \left(\frac{k^2}{3a^2 H^2} - x^2 + 1 \right) - \Omega_m\omega + y^2 \right] \Phi \\ & + \frac{\sqrt{3}x}{2}(c_s^2 - 1)\delta\phi' - \frac{3\sqrt{2}\lambda y^2}{4}(c_s^2 + 1)\delta\phi = 0 \quad (32) \end{aligned}$$

$$\begin{aligned} & \delta' + 3(\omega - c_s^2)(\sqrt{6}\alpha\beta x - 1)\delta + \frac{2}{3} \frac{k^2}{a^2 H^2 \Omega_m} \Phi + \left(-3\omega - 3 + \frac{k^2}{a^2 H^2 \Omega_m} \right) \Phi' \\ & - \frac{1}{\sqrt{2}}\alpha\beta(3\omega - 1)\delta\phi' + \sqrt{3} \left[\alpha\beta^2\gamma(3\omega - 1) - \frac{1}{9} \frac{k^2}{a^2 H^2 \Omega_m} \right] x\delta\phi = 0, \quad (33) \end{aligned}$$

where, ω and c_s denote the equation of state and sound speed of the dark matter fluid, respectively. We solve these equations for the redshift range $0 \leq z \lesssim 1500$. The calculations are done in the rest frame of the pressureless dark matter fluid, for which $\omega = c_s^2 = 0$ (cf. Appendix C). As mentioned in Sec II, this analysis is done for $U(\phi) \sim 1/\phi$ and $\alpha(\phi) \sim \phi$.

Analysis is also done for $n = 2$, however, the results are not sensitive to n . For completeness, in Appendix B, we have presented the results for $n = 2$.

To understand the effect of the interaction between dark energy and dark matter on the perturbed quantities, we define scaled interaction function δq :

$$\delta q = \frac{\delta Q}{H^3 M_{Pl}^2}. \quad (34)$$

Fig. 4 is the plot of δq as a function of number of e-foldings (N) for different k values. Since

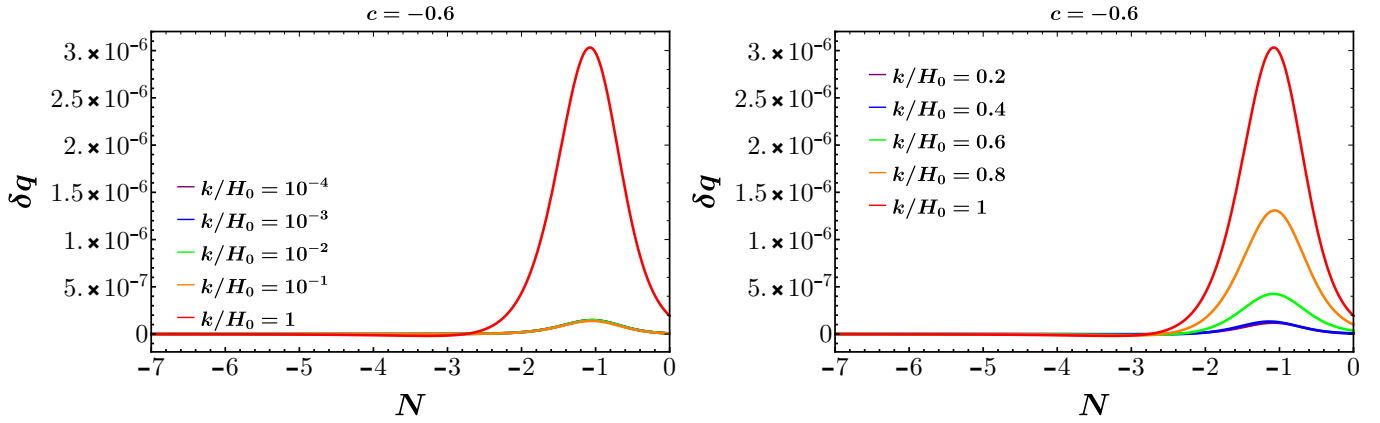


FIG. 4: Evolution of δq as a function of N for different values of k .

this forms the basis of the rest of the analysis, we would like to stress the following points: First, we see that the interaction function peaks around $N \sim -1$ ($z \sim 1.5 - 2.5$), and the interaction increases with increasing values of k . Second, since the interaction in the dark sector is a local interaction, the effect of the interaction should be least at the largest length scales (smallest k), and this is what we see from the plots. In other words, the interaction strength introduces a new length scale in the dynamics and leads to a preference for the growth of perturbations in certain length scales. We will see this feature for all the three quantities δ_m , $\Phi + \Psi$ and $\Phi' + \Psi'$.

In the following subsections, we obtain the evolution of the perturbed quantities relevant to the upcoming cosmological observations and determine the constraints to distinguish the interacting dark sector model from standard cosmology.

A. Structure formation

Over the last few decades, the three-dimensional distribution of galaxies is available due to many surveys. With the redshift measurement of millions of galaxies, there are two key conclusions: First, if we smoothen the distribution on the largest scales, it approaches a homogeneous distribution consistent with the FRW model. Second, in the smaller scales, there are overdense regions (clusters) and underdense regions (voids); around 10 Mpc, the RMS density-fluctuation amplitude is of the order unity. Since the interaction function, δq increases with increasing values of k , we can expect that the cold matter density perturbations in our model may have a different profile compared to standard cosmology.

Hence, first we look at the evolution of the matter density perturbation δ_m . More specifically, δ_m , $\Delta\delta_m$ and $\Delta\delta_{m_{rel}}$ defined in Eq. (29a). Figures 5 and 6 [7 and 8] contain plots of δ_m [$\Delta\delta_m$, $\Delta\delta_{m_{rel}}$] as a function of N for different length scales in interacting and non-interacting scenarios.

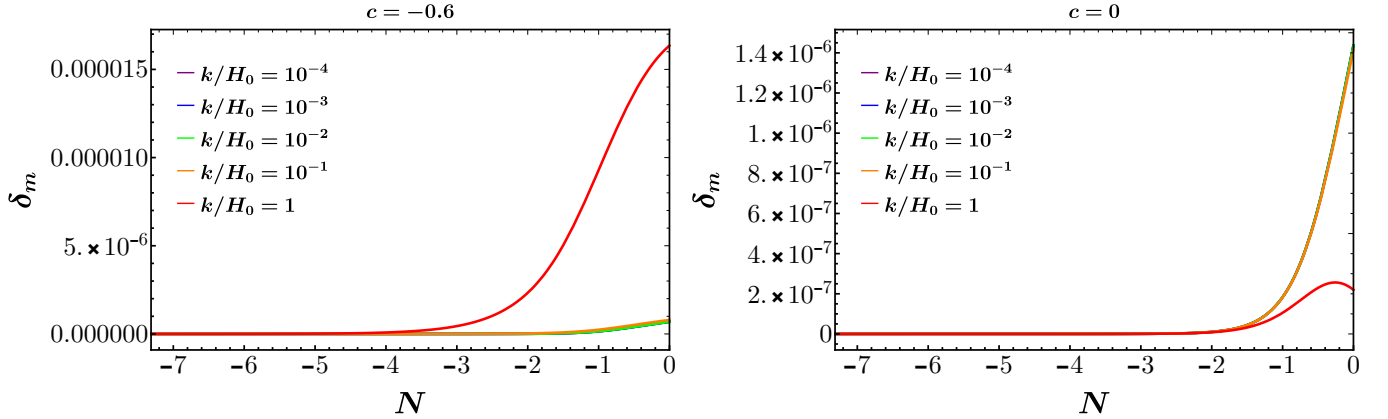


FIG. 5: Evolution of δ_m as a function of N . Left: $c = -0.6$, Right: $c = 0$.

From these plots, we infer the following: First, the difference in the evolution of δ_m between the interacting and non-interacting scenarios is significant after $N \sim -3$. Second, this difference increases with the increase in the value of the wavenumber k . This means that the interaction has a larger effect on the evolution of the scalar perturbations in the smaller length scales (large values of k) compared to the larger length scales (smaller values of k). Third, these deviations become significant for $z \sim 10 - 20$ and lie in the epoch of reionization. During this epoch, a predominantly neutral intergalactic medium was ionized by the emergence of the first luminous sources. Before the reionization epoch, the formation and

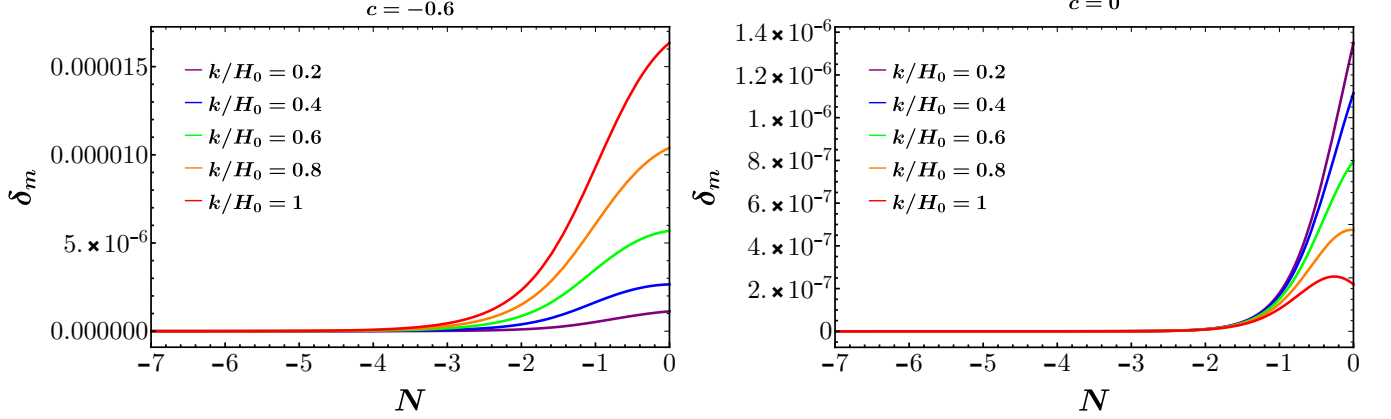


FIG. 6: Evolution of δ_m as a function of N . Left: $c = -0.6$, Right: $c = 0$.

evolution of structure were dominated by dark matter alone. However, the interacting dark sector leads to the exchange of density perturbations at smaller length scales. This indicates that it will be possible to detect the signatures of dark energy - dark matter interaction in the large scale structure observations. This provides a possible way to detect the signatures of dark sector interaction in the existing and upcoming cosmological observations like Euclid satellite [95], GMRT, SKA [96] and LOFAR [97] .

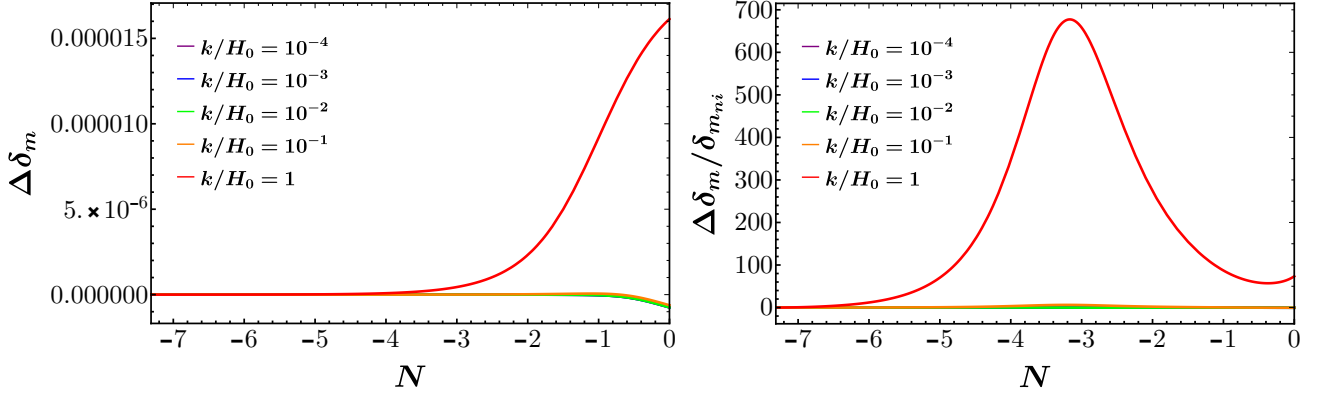


FIG. 7: Evolution of $\Delta\delta_m$ (left), $\Delta\delta_m/\delta_{m_{ni}}$ (right) as a function of N .

B. Weak gravitational lensing

The matter content of the Universe is dominated by dark matter. Most of the cosmological observations to study the matter distribution in the Universe depend on the observations of the luminous matter, which gives us little information regarding the total mass distribu-

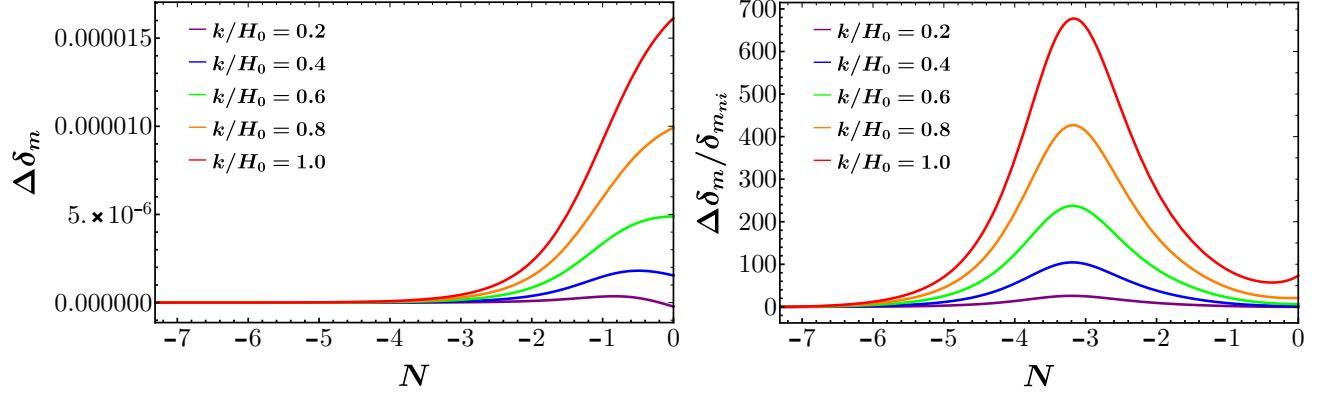


FIG. 8: Evolution of $\Delta\delta_m$ (left), $\Delta\delta_m/\delta_{m_{ni}}$ (right) as a function of N .

tion in the Universe. Gravitational lensing provides important information regarding the total mass distribution in the Universe, as it is independent of the nature of the matter and its interaction with electromagnetic radiation. Hence, weak gravitational lensing holds enormous promise as it can reveal the distribution of dark matter independently of any assumptions about its nature. The quantity $\Phi + \Psi$ determines the geodesic of a photon, which affects the weak gravitational lensing [7]. Like the standard cosmology, for the dark-sector interacting model considered here, $\Phi(t, x, y, z) = \Psi(t, x, y, z)$. Hence, it is sufficient to study the evolution of Φ to distinguish dark sector model with standard cosmology.

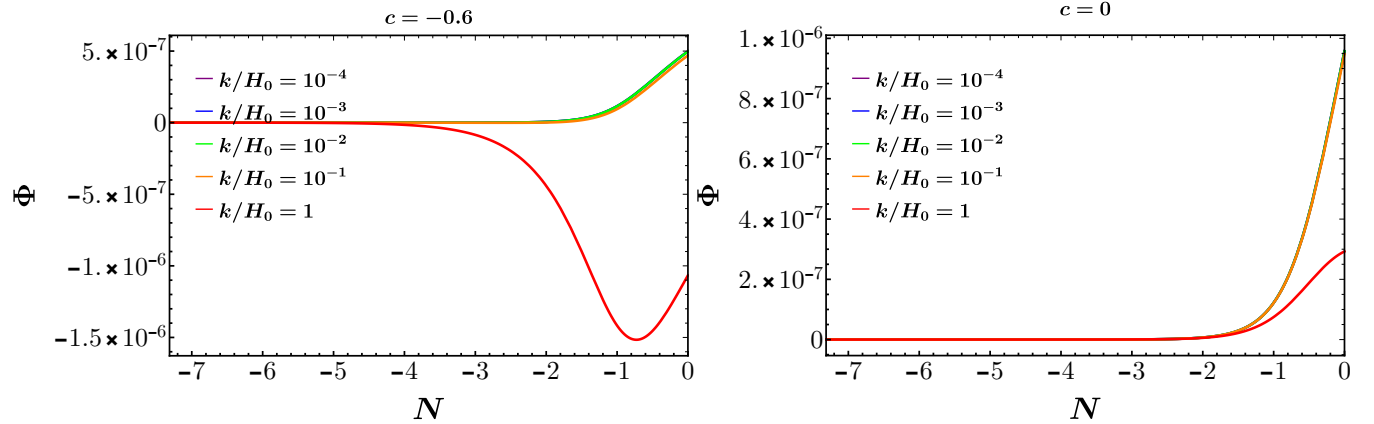


FIG. 9: Evolution of Φ as a function of N . Left: $c = -0.6$, Right: $c = 0$.

To study the signatures of the interacting dark sector, we look at the evolution of scalar metric perturbation Φ for different length scales starting from $z \sim 1500$. To analyze the difference in the evolution of Φ in the two scenarios, we also look at $\Delta\Phi$ and $\Delta\Phi_{rel}$. Figures 9 and 10 contain plots of Φ as a function of N for different length scales in interacting and

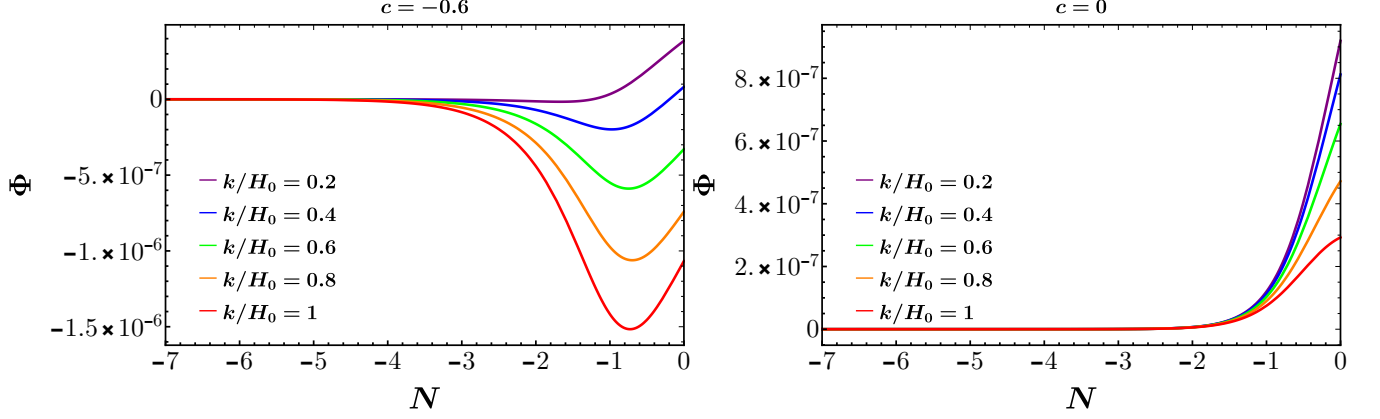


FIG. 10: Evolution of Φ as a function of N . Left: $c = -0.6$, Right: $c = 0$.

non-interacting scenarios. Evolution of $\Delta\Phi$ and $\Delta\Phi_{rel}$ as a function of N are plotted in Figures 11 and 12.

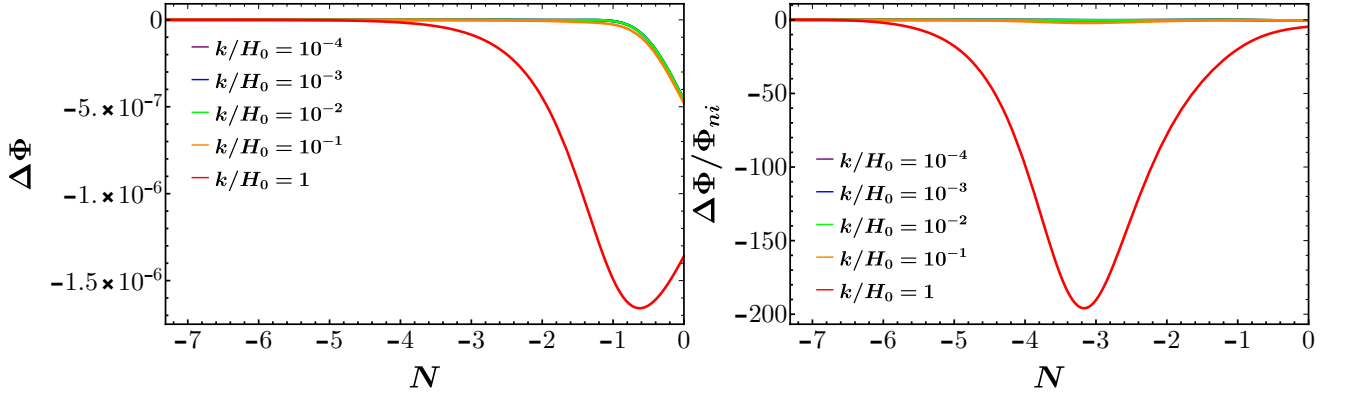


FIG. 11: Evolution of $\Delta\Phi$ (left), $\Delta\Phi/\Phi_{ni}$ (right) as a function of N .

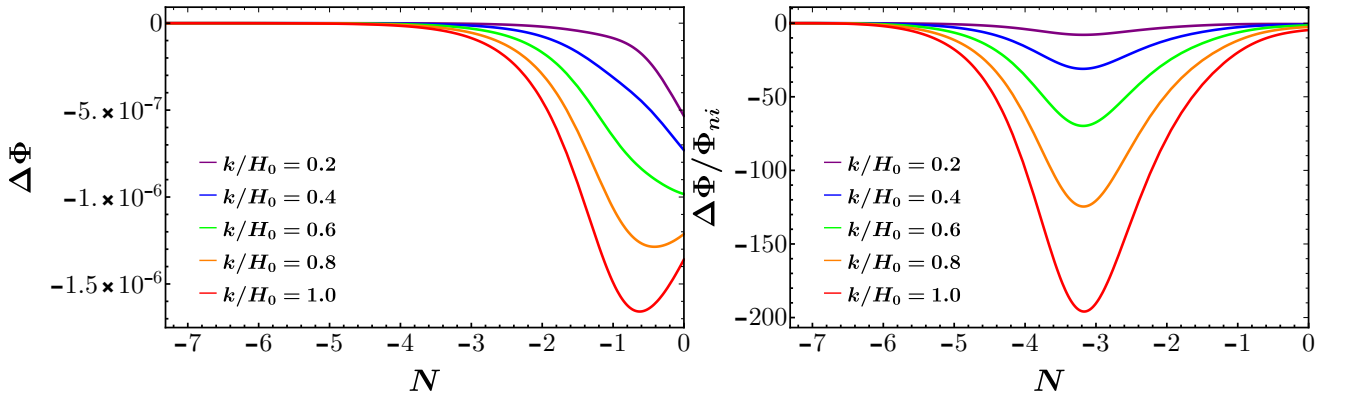


FIG. 12: Evolution of $\Delta\Phi$ (left), $\Delta\Phi/\Phi_{ni}$ (right) as a function of N .

From the evolution of these quantities, we see that starting from the same initial conditions at $z \sim 1500$, the evolution of Φ begins to show the effect of dark energy - dark matter interaction at about $N \sim -3$. This effect becomes even more prominent towards the lower redshifts $z < 5$. By looking at the k -dependence of the evolution, this effect is enhanced at lower length scales. This means that the interaction has a larger effect on the evolution of the scalar perturbations in the smaller length scales (large values of k) compared to the larger length scales (smaller values of k). Thus, this indicates that observations of weak lensing can help us potentially distinguish between interacting and non-interacting scenarios and potentially provide a way to resolve the tension between Planck-2018 and KiDS-450 in the $\sigma_8 - \Omega_m$ plane [98].

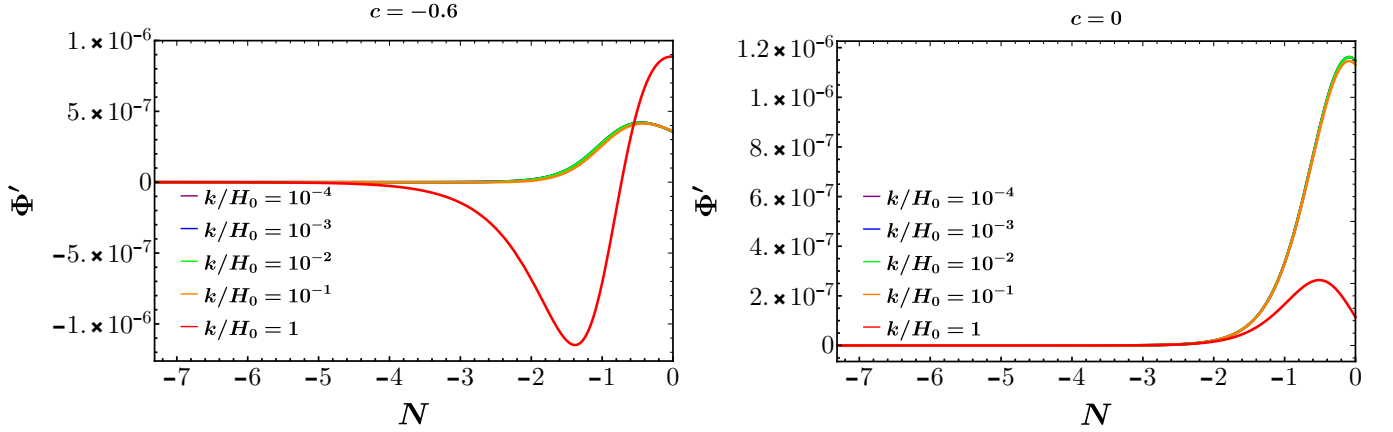


FIG. 13: Evolution of Φ' as a function of N . Left: $c = -0.6$, Right: $c = 0$.

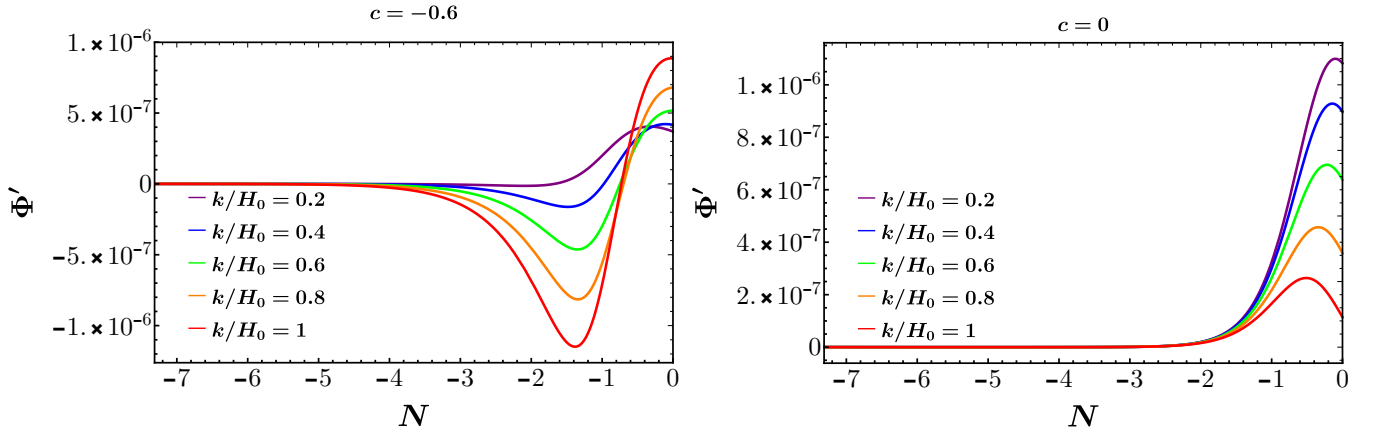


FIG. 14: Evolution of Φ' as a function of N . Left: $c = -0.6$, Right: $c = 0$.

C. Integrated Sachs-Wolfe effect

The integrated Sachs-Wolfe (ISW) effect is a secondary anisotropy of the cosmic microwave background (CMB), which arises because of the variation in the cosmic gravitational potential between local observers and the surface of the last scattering [99]. The ISW effect is related to the rate of change of $(\Phi + \Psi)$ w.r.t. conformal time (η) [7]. While weak gravitational lensing is determined by the spatial dependence of the metric scalar perturbation Φ , the ISW effect provides valuable information about the time evolution of the same, especially in the late accelerating Universe. Even though its detectability is weaker than weak lensing, it is a powerful tool to study the underlying cosmology. It can be detected using the cross-correlation between the observational data on CMB and large scale structures. In the flat Λ -CDM model, detection of the ISW signal provides direct detection of dark energy [100].

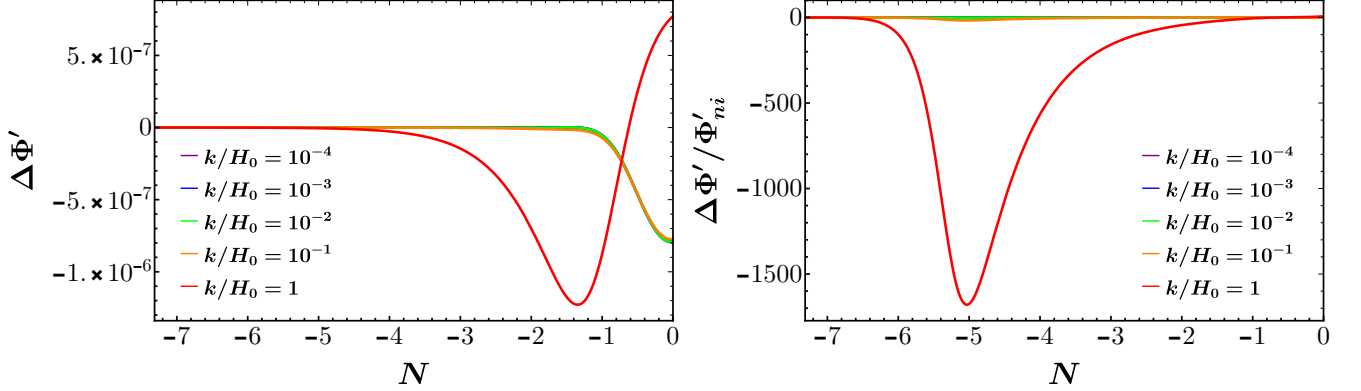


FIG. 15: Evolution of $\Delta\Phi'$ (left), $\Delta\Phi'/\Phi'_{ni}$ (right) as a function of N .

Since the Bardeen potential Φ evolve differently in the interacting and non-interacting scenarios, this change should potentially change the temperature fluctuations of the CMB photons. Figures 13 and 14 contain plots of Φ' as a function of N for different length scales in interacting and non-interacting scenarios. Evolution of $\Delta\Phi'$ and $\Delta\Phi'_{rel}$ as a function of N are plotted in Figures 15 and 16.

Like δ_m and Φ , we see that the difference in the evolution of Φ' in these two scenarios becomes significant at $N \sim -3$. Consistent with the fact that the first-order interaction term is larger at the smaller length scales, the difference in the evolution of Φ' in the interacting and non-interacting scenarios is enhanced for larger values of k . This indicates

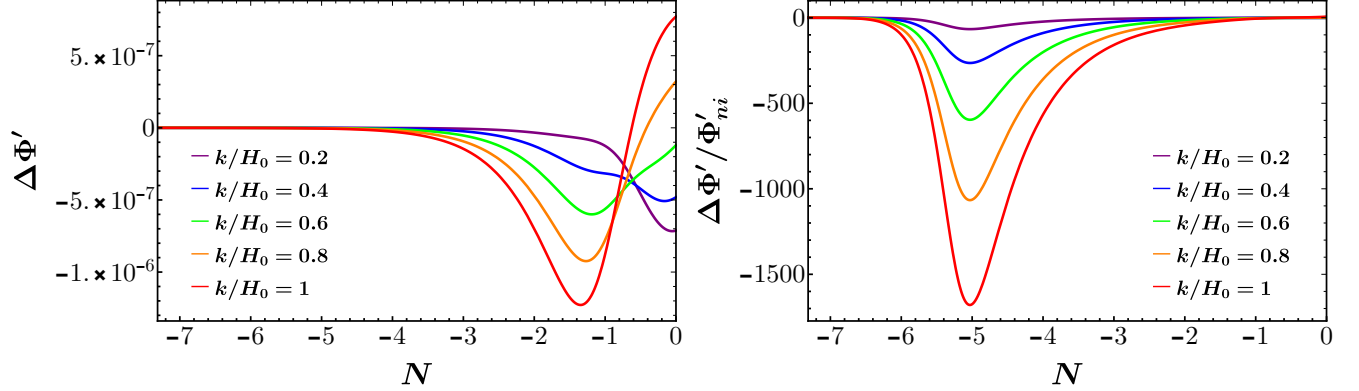


FIG. 16: Evolution of $\Delta\Phi'$ (left), $\Delta\Phi'/\Phi'_{ni}$ (right) as a function of N .

that observations on the ISW effect can detect or constrain dark energy and dark matter interaction.

V. CONCLUSIONS

In Ref. [46] two of the current authors found a mapping between phenomenological models of the dark-energy dark matter coupling functions Q from a consistent classical field theory. It was shown that the mapping holds both at the background and first-order perturbations level. In this work we used this interacting field theory framework for a specific scalar field potential $U(\phi) \sim 1/\phi^n$ and linear interaction function $\alpha(\phi) \sim \phi$. We analyzed the background cosmological evolution in this model and obtained the model parameters from cosmological observations. We evolved the perturbed equations in the redshift range $1500 \lesssim z \leq 0$ and obtained testable predictions of the model with future cosmological observations.

Constraints from observations: We obtained constraints for the model parameters from four observational data sets — Hubble parameter measurements, baryon acoustic oscillation observation, high- z HII galaxy measurements, and Type Ia supernovae observations. For numerical analysis, we rewrote the evolution equations in terms of dimensionless variables. Using the χ^2 minimization technique, we obtained the constraints on H_0 , Ω_m , w_0 , and the interaction strength C .

The key conclusions of the analysis for $n = 1$ ($U(\phi) \sim \phi^{-1}$) case are: (i) All the four data sets constrain the value of H_0 to be close to $70 \text{ km s}^{-1}\text{Mpc}^{-1}$. BAO+Hz and SN+Hz observations provide the tightest constraints, followed by HIIG and Hz measurements. (ii)

When a combined analysis of all four data sets is performed, the constraints are impacted by BAO and SN observations the most, and the allowed range for H_0 becomes even narrower. (iii) The constraints on Ω_m obtained from various data sets are consistent with each other, and BAO+Hz provides the smallest allowed range, which drives the limit for combined analysis, followed by SN + Hz, Hz, and then HIIG data. (iv) When it comes to constraining w_0 , all the observations are consistent with the Λ CDM model, and only Hz data allows for a non-accelerating universe. (v) As for the constraints on C , we find that only BAO+Hz data constrains C within 3σ confidence region, and hence, when analysis with a combination of the data sets is performed, the allowed values of C is influenced by BAO+Hz data the most. We also find that, except for Hz measurements, all the three data sets show a preference for a negative value C (cf. Table II). The Hz data is nearly insensitive to the sign and value of C within the considered range.

The key conclusions of the analysis for $n = 2$ ($U(\phi) \sim \phi^{-2}$) case are: (i) Constraints from Hz data set does not change significantly, for other data sets, there is a slight shift of the contours. (ii) The observations prefer slightly higher values of Ω_m , the contours from Hz data shifts towards higher values of Ω_m . HIIG data allows a significantly larger range of Ω_m compared to $n = 1$. For SN+Hz observations, there is no significant change in the lower range but the upper limit on Ω_m shifts slightly higher. For BAO+Hz data, the change in the allowed range of Ω_m is insignificant. (iii) For H_0 , the change is not noticeable when we go from $U(\phi) \sim \phi^{-1}$ to ϕ^{-2} . For w_0 , from Hz data, there is no noticeable change, but the allowed ranges increase when the $n = 1$ is changed to $n = 2$ for BAO+Hz, HIIG, and SN+Hz observations. (iv) The constraints on coupling parameter C changes significantly when n changes. For $n = 2$, constraints on C from Hz do not show much change. Still, for BAO+Hz, HIIG, and SN+Hz data, we get an upper limits on C , and the contours shift towards negative values of C , showing their preference for a negative value of interaction strength. We can also see this in constraints obtained from the combination of data sets. All the observations are consistent with $C = -1$, but BAO+Hz, HIIG, and SN+Hz observations do not agree with $C = 1$ within 1σ confidence regions for $n = 2$ case.

Distinguishing dark sector interacting model from standard cosmology: To distinguish the interacting dark sector from the non-interacting dark sector, we looked at the evolution of the scalar perturbations in the interacting dark sector model. We considered a inverse potential $U(\phi) \sim 1/\phi$ and a linear interaction function $\alpha(\phi) \sim \phi$ with negative

values of interaction strength C . We evolved three perturbed quantities (δ_m, Φ, Φ') from last scattering surface to present epoch ($1500 \lesssim z \leq 0$). These three perturbed quantities are related to structure formation, weak gravitational lensing, and the ISW effect, respectively.

The density perturbation δ_m grows faster in the interacting scenarios, especially at the lower length scales. The difference in the evolution becomes significant for $z < 20$, for all length scales, and the difference peaks at smaller redshift values $z < 5$. This means that cosmological observations related to the formation of large scale structures can potentially detect the signatures of dark matter - dark energy interaction. We see a similar trend in the evolution of Φ and Φ' as well, which indicates an interaction between dark energy and dark matter will be reflected on the observational data on weak gravitational lensing and ISW effect. We get a similar behaviour for inverse-square potential $U(\phi) \propto 1/\phi^2$. The evolution of the perturbations in the interacting dark sector also differ from the ones in modified gravity models like $f(R)$ gravity, which describes the late time acceleration of the Universe[101].

It is interesting to note that all the perturbed quantities significant for $z \sim 10 - 20$ and lie in the epoch of reionization. During this epoch, a predominantly neutral intergalactic medium was ionized by the emergence of the first luminous sources. Before the reionization epoch, the formation and evolution of structure were dominated by dark matter alone. However, the interacting dark sector leads to the exchange of density perturbations at smaller length scales. This indicates that it is possible to distinguish these models from the observations at the epoch of reionization.

We have shown that the dark sector interaction mode can alleviate the tension between Planck measurements and cosmological probes. The constraints on the dark energy-dark matter interaction model parameters can be used as priors in future studies. We have not addressed the issue of the tension in the $\sigma_8 - \Omega_m$ plane between Planck and cosmic shear experiments [98]. We plan to address this in future work.

Currently, we are looking to obtain the constraints on the model from the evolution of the perturbations using the relevant observational data sets. It will also be interesting to look at the observational consequences of the difference in the evolution of the density perturbation. Since interaction is higher for the smaller length scales, it can significantly affect the evolution of the mass distribution of the binary black holes detected by the gravitational wave observations [102].

VI. ACKNOWLEDGEMENTS

We thank T. Padmanabhan for fruitful discussions. We thank Ana Luisa González-Morán for providing Gordon extinction corrected HIIG measurements and useful information related to the measurements. JPJ is supported by CSIR Senior Research Fellowship, India. The work is partially supported by the ISRO-Respond grant.

Appendix A: Parameter constraints for $U(\phi) \sim 1/\phi^2$

For completeness, in this Appendix, we present the constraints for $n = 2$ in the quintessence potential (10). Note that in Sec. IIIC, we presented the detailed analysis for $n = 1$. As mentioned earlier, the parameter constraints are roughly the same for $n = 1$ and $n = 2$. Figures 17 and 18 contain the constraints on parameters H_0 , interaction strength C , and Ω_m for the four observational data sets — Hz, BAO, HIIG, and SN.

Here are the key inferences from Figures 17 and 18: (i) For $n = 2$, the constraints on H_0 , w_0 and C obtained from the data sets are almost same as for $n = 1$. (ii) From Hz data, the minimum value of χ^2 is 18.77 which corresponds to the best fit values of the parameters are $H_0 = 69.37 \text{ km s}^{-1}\text{Mpc}^{-1}$, $\Omega_m = 0.29$, $w_0 = -0.98$ and the interaction strength is $C = 0.98$. (iii) For BAO+Hz data, when it comes to the interaction strength C the preference for negative value is more evident here than for $n = 1$. Although for $1/\phi^2$ potential, the data does not allow for a non-accelerating universe, a larger range for w_0 is obtained. (iii) For HIIG observations, $n = 2$ provides a larger range of parameters than $n = 1$. (iv) For SN+Hz data, the H_0 and Ω_m constraints are as narrow as in $n = 1$ case, but the observations prefer negative value for C .

From Figure 18 we see that the four data sets do not provide a lower limit on w_0 . Hz data provides an upper limit of -0.68 within 1σ and $w_0 = 0.03$ within 3σ region, showing that this particular model does not allow for a non-accelerating universe within 1σ region. The allowed ranges are almost the same as in the case $n = 1$.

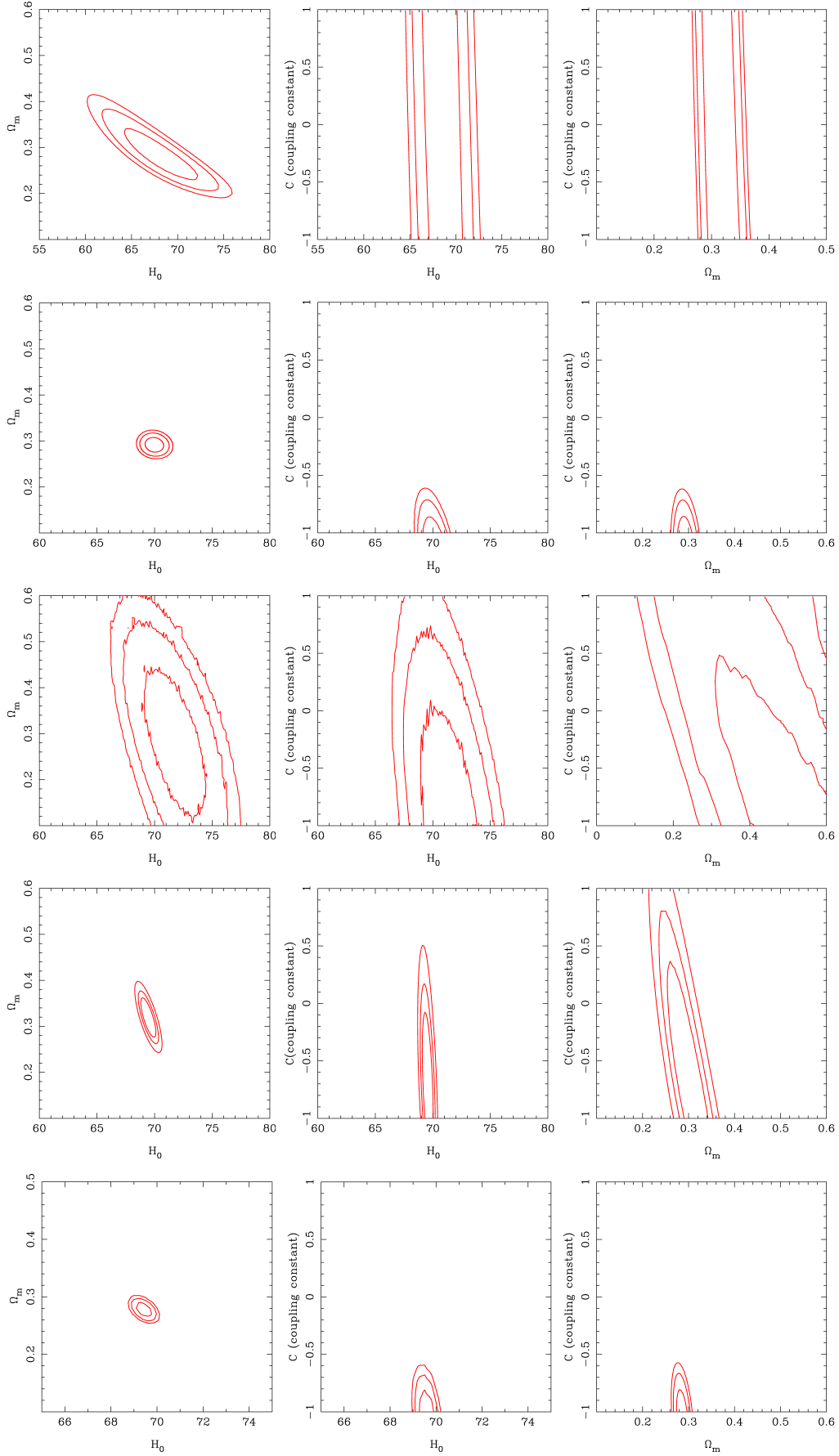


FIG. 17: 1,2,3- σ likelihood contours for Hz data (I row), BAO+Hz data (II row), HIIG data (III row), SN+Hz data (IV row) and all four data sets (V row). The two-dimensional contours are obtained by performing marginalization over other parameters.

BAO+Hz observation does not allow for a non-accelerating Universe within the 3σ region, and the allowed range for w_0 is wider as compared to the $n = 1$ case. The HIIG data also allows a wider range for w_0 of -0.83 within the 3σ region and allows the entire range of Ω_m considered in the analysis. The SN+Hz data also allows a wider range for w_0 and Ω_m as compared to $n = 1$ case. Apart from Hz data, the three remaining observational data sets considered in the analysis do not allow for a non-accelerating universe for both $n = 1$ and 2. For w_0 , Hz observations provide the widest allowed range within 3σ confidence level.

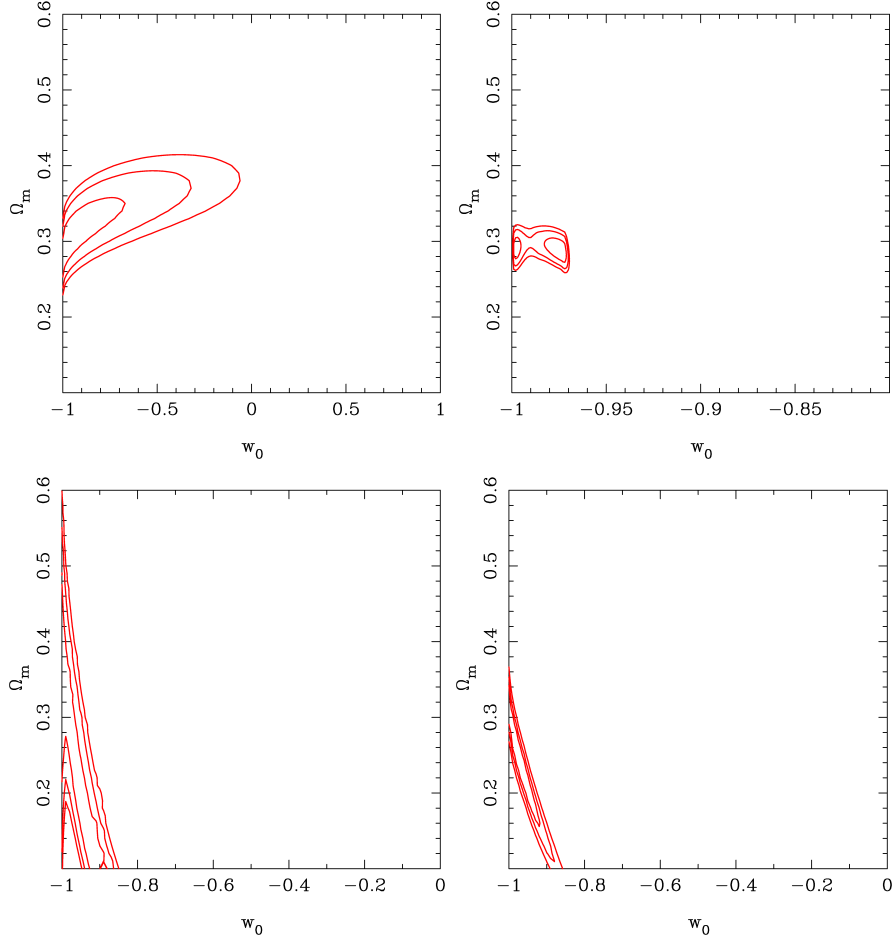


FIG. 18: 1,2,3- σ likelihood contours in ‘ w_0 - Ω_m ’ plane. The top row shows constraints from Hz data (left) and BAO+Hz observations (right). The second row shows constraints from HIIG measurements (left) and SN+Hz observations (right).

Appendix B: Evolution of scalar perturbations for ϕ^{-2} potential

For completeness, in this Appendix, we present the evolution of the matter density perturbation δ_m and related quantities for $n = 2$ in the quintessence potential (10). Note that in Sec. IV, we presented the detailed analysis for $n = 1$. As mentioned earlier, the evolution of the perturbed quantities is not sensitive to n .

1. Evolution of the scaled interaction function δq

Fig. 19 is the plot of δq (cf. Eq. 34) as a function of N for different k values. Comparing this plot with the plots in Fig. 4, we see that evolution of the interaction function is roughly the same for the both the cases. Hence, the evolution of scaled interaction function δq is not sensitive to n .

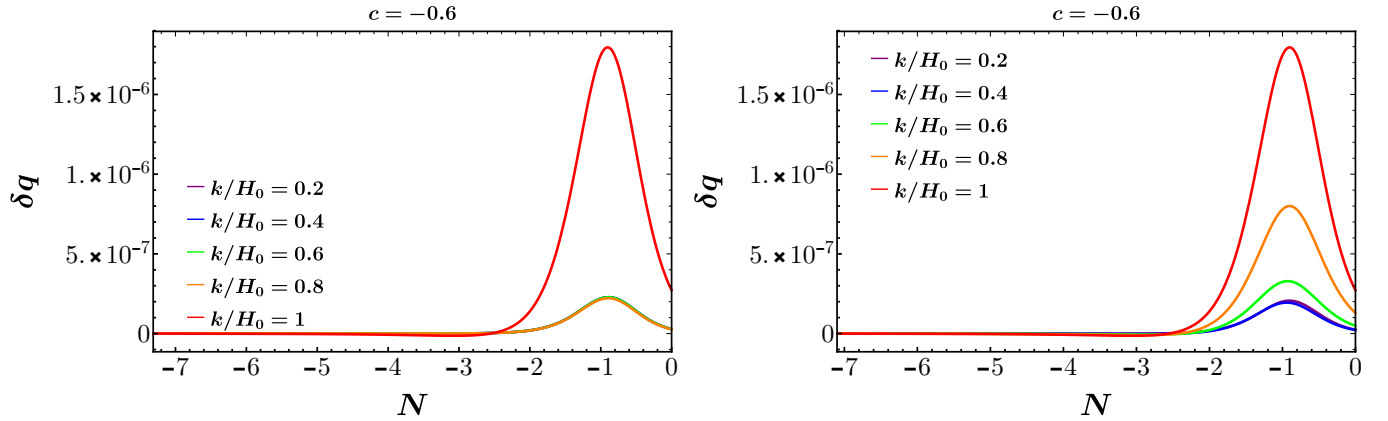


FIG. 19: Evolution of δq as a function of N for different values of k ;

2. Structure formation

Figures 20 and 21 contain plots of δ_m as a function of N for different length scales in interacting and non-interacting scenarios. Figures 22 and 23 contain the plots of $\Delta\delta_m$ and $\Delta\delta_{m_{rel}}$ as a function of N for different length scales, respectively. Thus, we see that evolution of δ_m is roughly the same for $n = 1$ and $n = 2$.

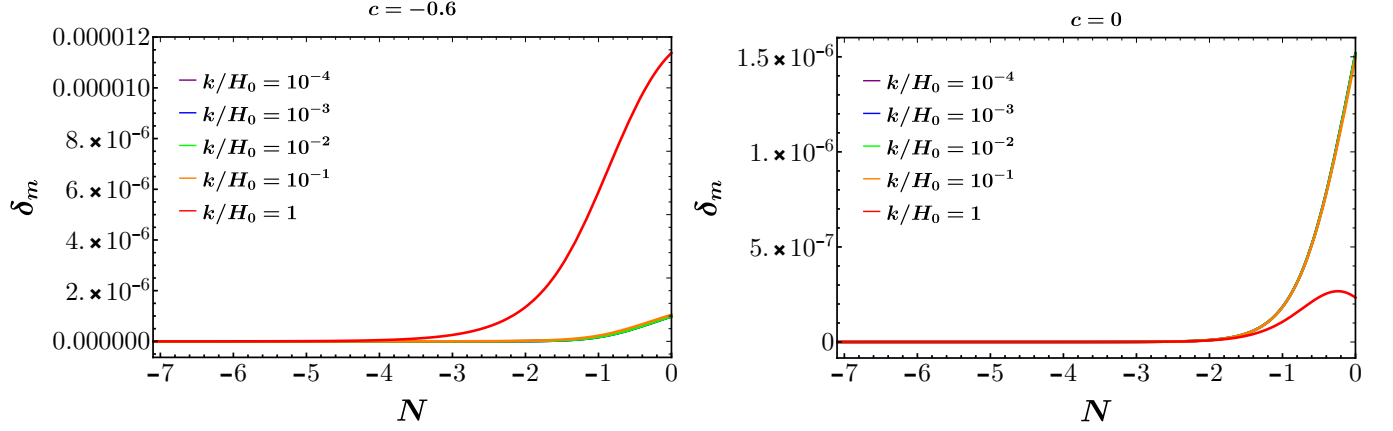


FIG. 20: Evolution of δ_m as a function of N . Left: $c = -0.6$, Right: $c = 0$.

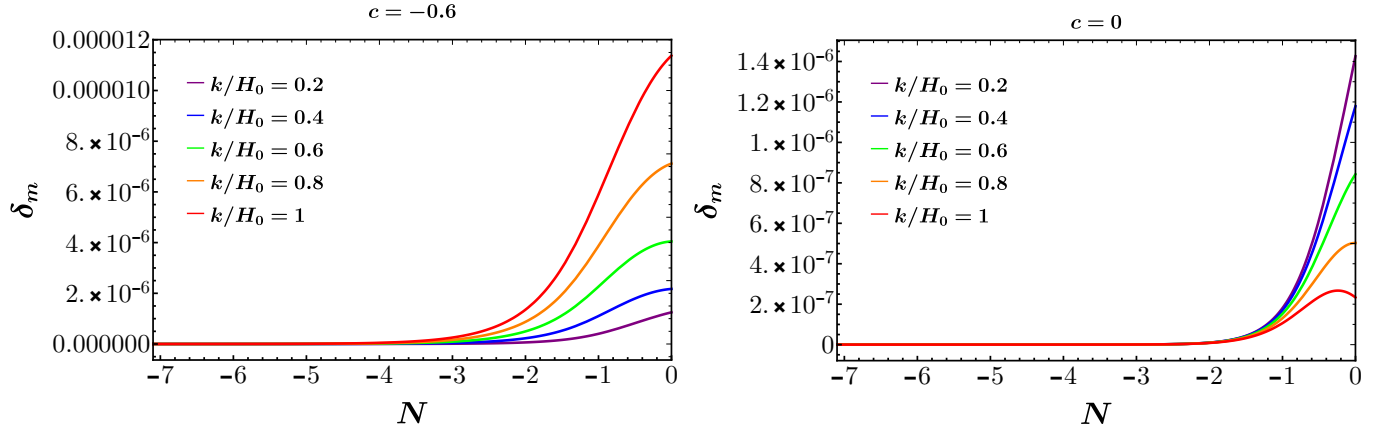


FIG. 21: Evolution of δ_m as a function of N . Left: $c = -0.6$, Right: $c = 0$.

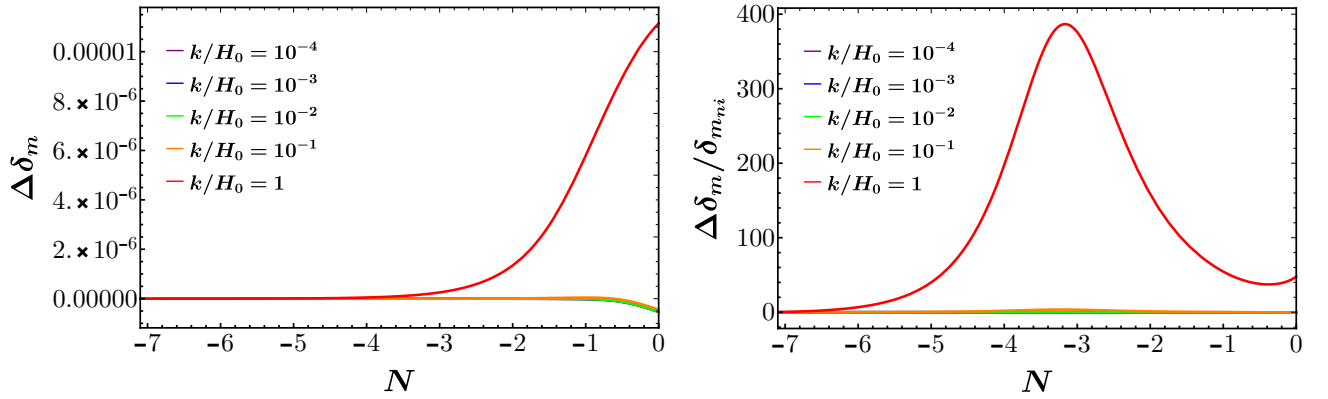


FIG. 22: Evolution of $\Delta\delta_m$ (left), $\Delta\delta_m/\delta_{mni}$ (right) as a function of N .

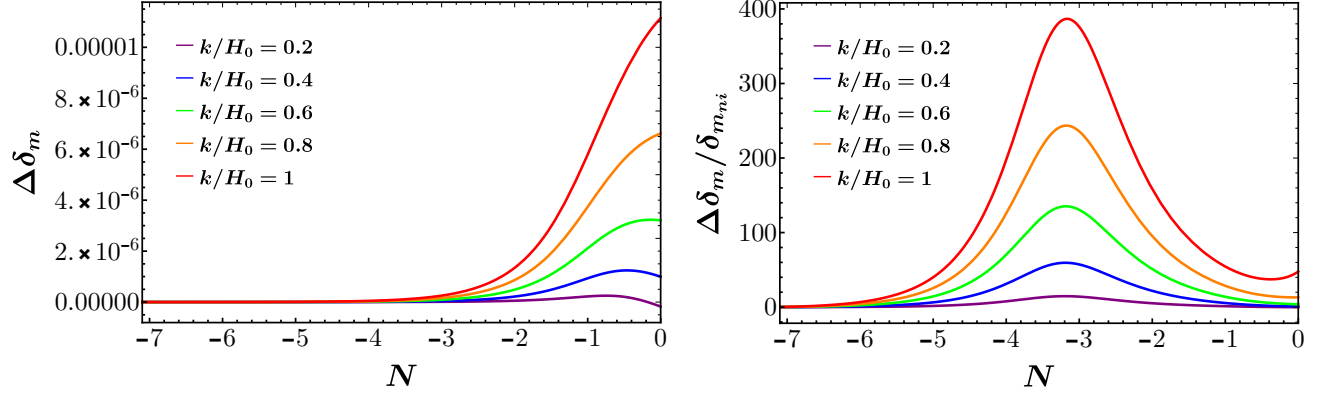


FIG. 23: Evolution of $\Delta\delta_m$ (left), $\Delta\delta_m/\delta_{m,ni}$ (right) as a function of N .

3. Weak gravitational lensing

Figures 24 and 25 contain plots of Φ as a function of N for different length scales in interacting and non-interacting Figures 26 and 27 contain the plots of $\Delta\Phi$ and $\Delta\Phi/\Phi_{ni}$ as a function of N for different length scales, respectively. Thus, we see that evolution of Φ is roughly the same for the both the cases and is not sensitive to n .

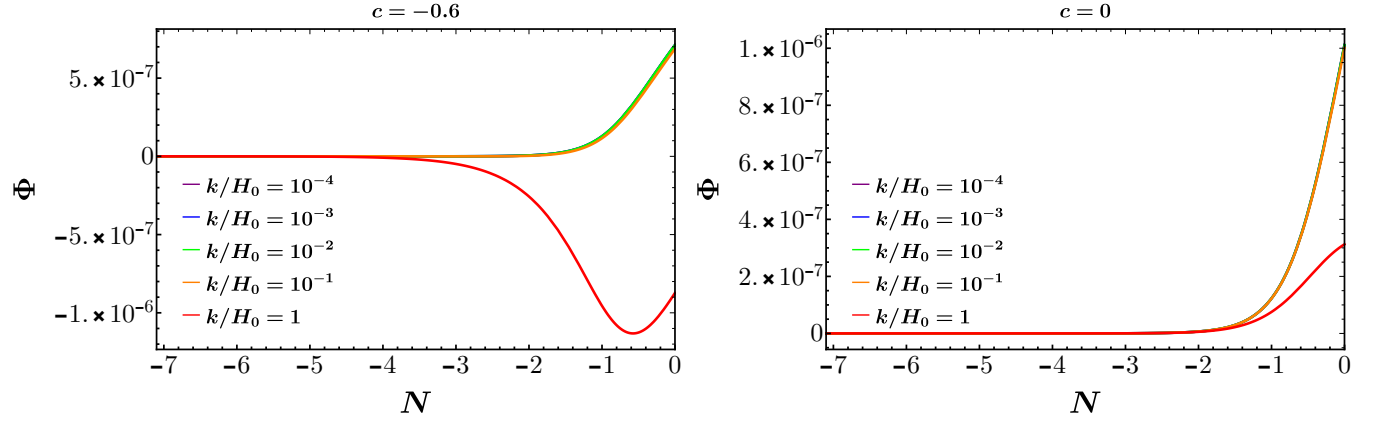


FIG. 24: Evolution of Φ as a function of N . Left: $c = -0.6$, Right: $c = 0$.

4. ISW effect

Figures 28 and 29 contain plots of Φ' as a function of N for different length scales in interacting and non-interacting Figures 30 and 31 contain the plots of $\Delta\Phi'$ and $\Delta\Phi'/\Phi'_{ni}$ as a function of N for different length scales, respectively. Thus, we see that evolution of Φ' is

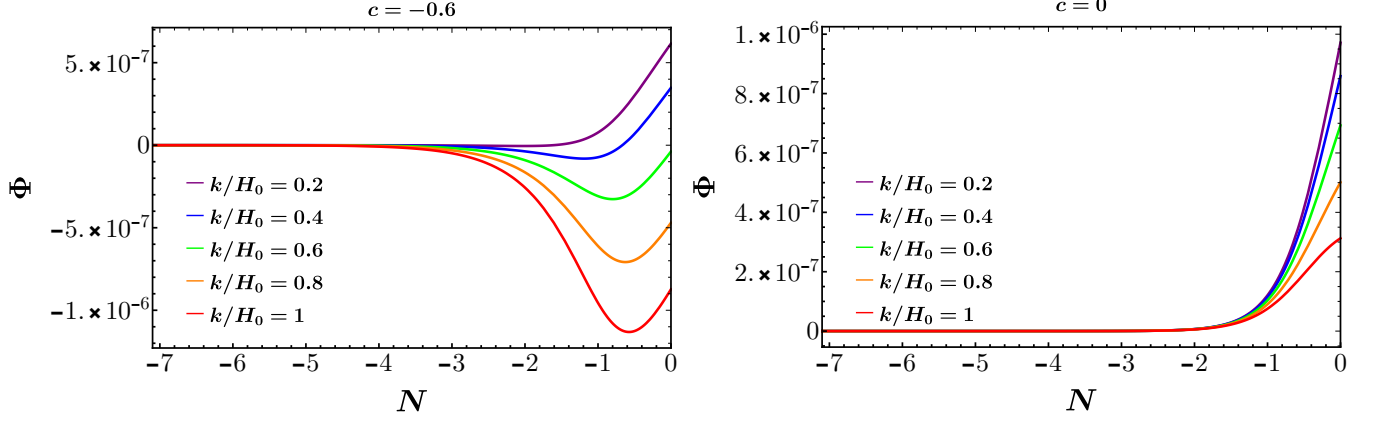


FIG. 25: Evolution of Φ as a function of N . Left: $c = -0.6$, Right: $c = 0$.

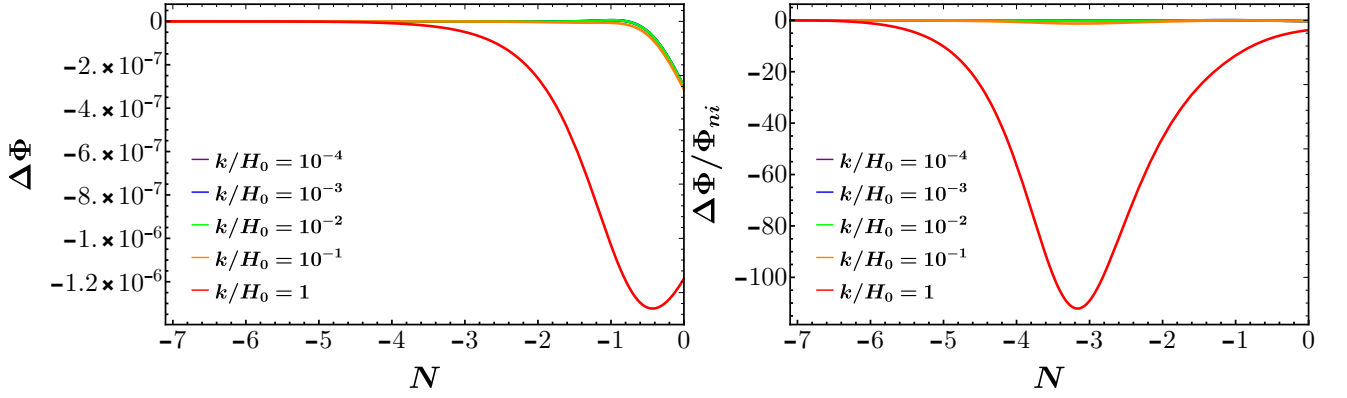


FIG. 26: Evolution of $\Delta\Phi$ (left), $\Delta\Phi/\Phi_{ni}$ (right) as a function of N .

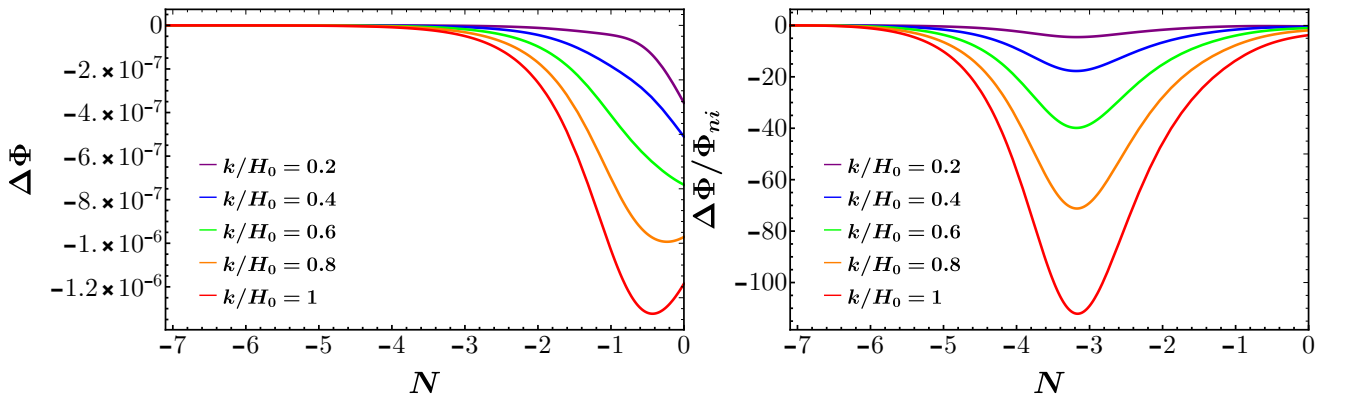


FIG. 27: Evolution of $\Delta\Phi$ (left), $\Delta\Phi/\Phi_{ni}$ (right) as a function of N .

roughly the same for the both the cases and is not sensitive to n .

We thus conclude that the evolution of δ_m , Φ and Φ' for the inverse square potential follow

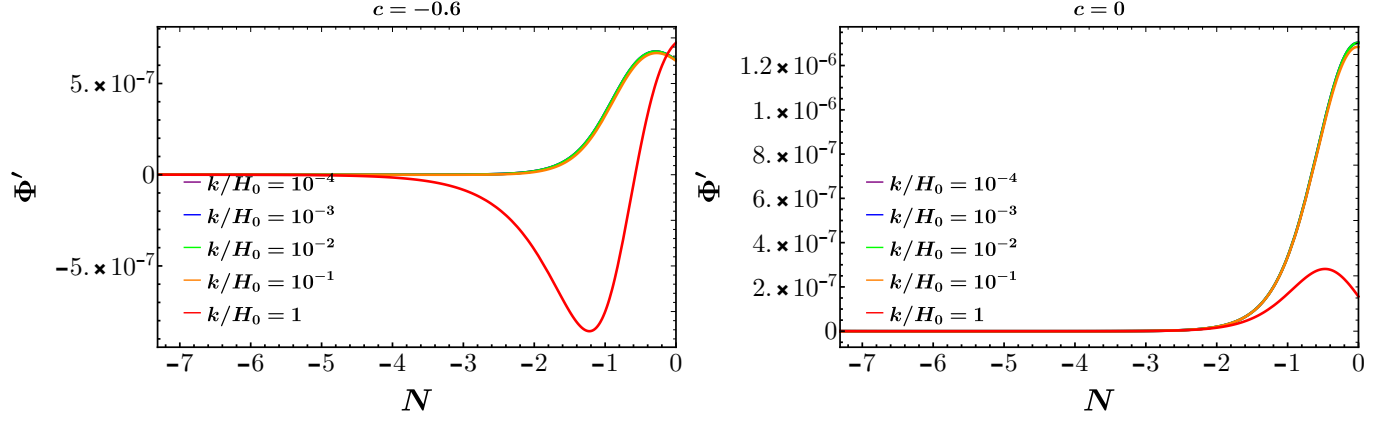


FIG. 28: Evolution of Φ' as a function of N . Left: $c = -0.6$, Right: $c = 0$.

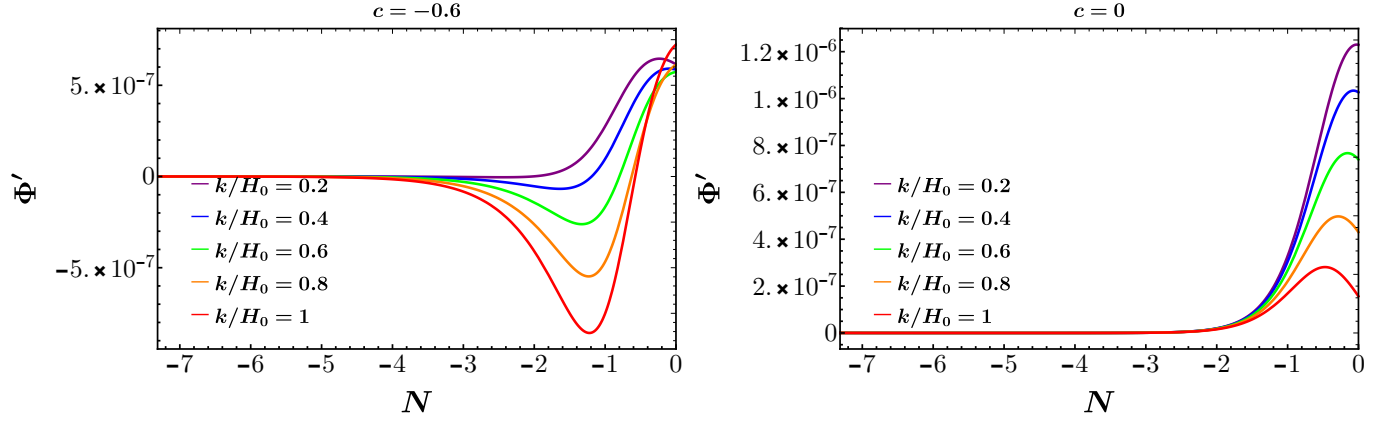


FIG. 29: Evolution of Φ' as a function of N . Left: $c = -0.6$, Right: $c = 0$.

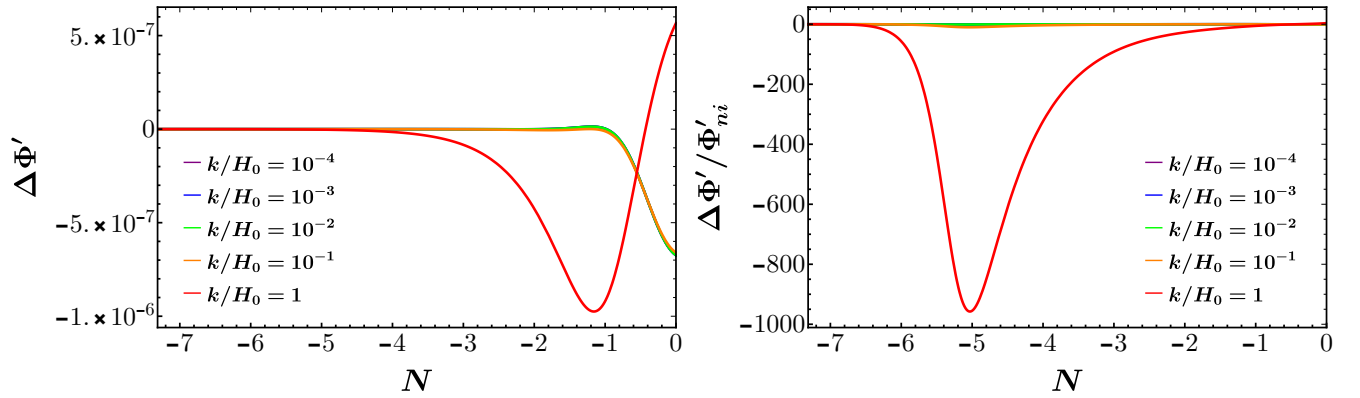


FIG. 30: Evolution of $\Delta\Phi'$ (left), $\Delta\Phi'/\Phi'_{ni}$ (right) as a function of N .

a similar trend as compared to the $U(\phi) \sim 1/\phi$ case. The difference in the evolution becomes significant for $z < 20$, for all length scales. This means that cosmological observations related

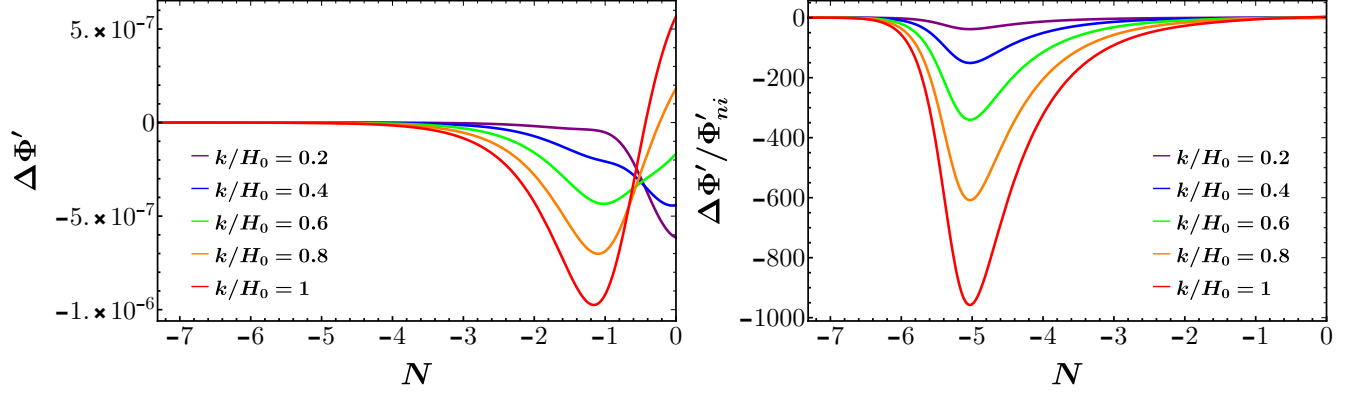


FIG. 31: Evolution of $\Delta\Phi'$ (left), $\Delta\Phi'/\Phi'_{ni}$ (right) as a function of N .

to the formation of large scale structures can potentially detect the signatures of dark matter - dark energy interaction.

Appendix C: Sound speed of the scalar field

Sound speed and adiabatic sound speed of the dark energy scalar field (ϕ) is given by [103]

$$c_s^2 = \frac{\delta p_\phi}{\delta \rho_\phi}, \quad c_{s_{ad}}^2 = \frac{\dot{p}_\phi}{\dot{\rho}_\phi} = -1 - \frac{2\ddot{\phi}}{3H\dot{\phi} + 2\alpha_\phi \bar{\rho}_m M_{Pl}^2} \quad (C1)$$

In terms of the dimensionless variables, these quantities can be expressed as

$$c_{s_{ad}}^2 = \frac{h'(x^2 - y^2) + h(xx' - yy')}{h'(x^2 + y^2) + h(xx' + yy')} = -1 - \frac{2(x' + \frac{h'}{h})}{\sqrt{3}(\sqrt{12}x - \sqrt{2}\alpha\beta\Omega_m)} \quad (C2)$$

$$c_s^2 = \frac{12\Phi x^2 - 2\sqrt{3}x\delta\phi' - 3\sqrt{2}\lambda y^2\delta\phi}{12\Phi x^2 - 2\sqrt{3}x\delta\phi' + 3\sqrt{2}\lambda y^2\delta\phi} \quad (C3)$$

For a quintessence model, $c_s^2 = 1$ in the rest frame of ϕ [104]. In this work, the perturbed quantities are evaluated in the dark matter rest frame.

-
- [1] A. G. Riess and Others, *Astron. J.* **116**, 1009 (1998), [arXiv:astro-ph/9805201 \[astro-ph\]](#).
 - [2] S. Perlmutter and Others, *Astrophys. J.* **517**, 565 (1999), [arXiv:astro-ph/9812133 \[astro-ph\]](#).
 - [3] D. N. Spergel and Others, *Astrophys. J. Suppl.* **170**, 377 (2007), [arXiv:astro-ph/0603449 \[astro-ph\]](#).

- [4] D. M. Scolnic and Others, *Astrophys. J.* **859**, 101 (2018), [arXiv:1710.00845 \[astro-ph.CO\]](#).
- [5] Y. Akrami and Others (Planck), *Astron. Astrophys.* **641**, A1 (2018), [arXiv:1807.06205 \[astro-ph.CO\]](#).
- [6] N. Aghanim *et al.* (Planck), *Astron. Astrophys.* **641**, A6 (2020), [arXiv:1807.06209 \[astro-ph.CO\]](#).
- [7] T. Padmanabhan, *Theoretical Astrophysics: Volume 3, Galaxies and Cosmology*, Theoretical Astrophysics (Cambridge University Press, 2000); V. Mukhanov, *Physical Foundations of Cosmology* (Cambridge University Press, 2005); S. Weinberg, *Cosmology*, Cosmology (OUP Oxford, 2008); D. S. Gorbunov and V. A. Rubakov, *Introduction to the Theory of the Early Universe* (World Scientific Publishing Company, 2011).
- [8] V. Marra, L. Amendola, I. Sawicki, and W. Valkenburg, *Phys. Rev. Lett.* **110**, 241305 (2013), [arXiv:1303.3121 \[astro-ph.CO\]](#).
- [9] L. Verde, P. Protopapas, and R. Jimenez, *Phys. Dark Univ.* **2**, 166 (2013), [arXiv:1306.6766 \[astro-ph.CO\]](#).
- [10] C. L. Bennett, D. Larson, J. L. Weiland, and G. Hinshaw, *Astrophys. J.* **794**, 135 (2014), [arXiv:1406.1718 \[astro-ph.CO\]](#).
- [11] B. Ratra and P. J. E. Peebles, *Phys. Rev. D* **37**, 3406 (1988).
- [12] E. J. Copeland, M. Sami, and S. Tsujikawa, *Int. J. Mod. Phys. D* **15**, 1753 (2006), [arXiv:hep-th/0603057 \[hep-th\]](#).
- [13] L. Amendola, *Mon. Not. Roy. Astron. Soc.* **312**, 521 (2000), [arXiv:astro-ph/9906073](#).
- [14] L. Amendola, *Phys. Rev. D* **62**, 043511 (2000), [arXiv:astro-ph/9908023](#).
- [15] A. P. Billyard and A. A. Coley, *Phys. Rev. D* **61**, 083503 (2000), [arXiv:astro-ph/9908224](#).
- [16] G. Olivares, F. Atrio-Barandela, and D. Pavon, *Phys. Rev. D* **71**, 063523 (2005), [arXiv:astro-ph/0503242](#).
- [17] L. Amendola, G. Camargo Campos, and R. Rosenfeld, *Phys. Rev. D* **75**, 083506 (2007), [arXiv:astro-ph/0610806](#).
- [18] G. Olivares, F. Atrio-Barandela, and D. Pavon, *Phys. Rev. D* **77**, 063513 (2008), [arXiv:0706.3860 \[astro-ph\]](#).
- [19] C. G. Boehmer, G. Caldera-Cabral, R. Lazkoz, and R. Maartens, *Phys. Rev. D* **78**, 023505 (2008), [arXiv:0801.1565 \[gr-qc\]](#).
- [20] G. Caldera-Cabral, R. Maartens, and L. Urena-Lopez, *Phys. Rev. D* **79**, 063518 (2009),

- [arXiv:0812.1827 \[gr-qc\]](#).
- [21] J.-H. He and B. Wang, *JCAP* **06**, 010 (2008), [arXiv:0801.4233 \[astro-ph\]](#).
 - [22] V. Pettorino and C. Baccigalupi, *Phys. Rev. D* **77**, 103003 (2008), [arXiv:0802.1086 \[astro-ph\]](#).
 - [23] M. Quartin, M. O. Calvao, S. E. Joras, R. R. Reis, and I. Waga, *JCAP* **05**, 007 (2008), [arXiv:0802.0546 \[astro-ph\]](#).
 - [24] C. G. Boehmer, G. Caldera-Cabral, N. Chan, R. Lazkoz, and R. Maartens, *Phys. Rev. D* **81**, 083003 (2010), [arXiv:0911.3089 \[gr-qc\]](#).
 - [25] J. Beyer, S. Nurmi, and C. Wetterich, *Phys. Rev. D* **84**, 023010 (2011), [arXiv:1012.1175 \[astro-ph.CO\]](#).
 - [26] L. Lopez Honorez, O. Mena, and G. Panotopoulos, *Phys. Rev. D* **82**, 123525 (2010), [arXiv:1009.5263 \[astro-ph.CO\]](#).
 - [27] P. Avelino and H. da Silva, *Phys. Lett. B* **714**, 6 (2012), [arXiv:1201.0550 \[astro-ph.CO\]](#).
 - [28] S. Pan, S. Bhattacharya, and S. Chakraborty, *Mon. Not. Roy. Astron. Soc.* **452**, 3038 (2015), [arXiv:1210.0396 \[gr-qc\]](#).
 - [29] V. Salvatelli, A. Marchini, L. Lopez-Honorez, and O. Mena, *Phys. Rev. D* **88**, 023531 (2013), [arXiv:1304.7119 \[astro-ph.CO\]](#).
 - [30] L. P. Chimento, M. G. Richarte, and I. E. Sánchez García, *Phys. Rev. D* **88**, 087301 (2013), [arXiv:1310.5335 \[gr-qc\]](#).
 - [31] L. Amendola, T. Barreiro, and N. J. Nunes, *Phys. Rev. D* **90**, 083508 (2014), [arXiv:1407.2156 \[astro-ph.CO\]](#).
 - [32] V. Marra, *Phys. Dark Univ.* **13**, 25 (2016), [arXiv:1506.05523 \[astro-ph.CO\]](#).
 - [33] F. F. Bernardi and R. G. Landim, *Eur. Phys. J. C* **77**, 290 (2017), [arXiv:1607.03506 \[gr-qc\]](#).
 - [34] S. Pan and G. Sharov, *Mon. Not. Roy. Astron. Soc.* **472**, 4736 (2017), [arXiv:1609.02287 \[gr-qc\]](#).
 - [35] C. Van De Bruck and J. Mifsud, *Phys. Rev. D* **97**, 023506 (2018), [arXiv:1709.04882 \[astro-ph.CO\]](#).
 - [36] M. Carrillo González and M. Trodden, *Phys. Rev. D* **97**, 043508 (2018), [Erratum: *Phys. Rev. D* 101, 089901 (2020)], [arXiv:1705.04737 \[astro-ph.CO\]](#).
 - [37] B. J. Barros, L. Amendola, T. Barreiro, and N. J. Nunes, *JCAP* **01**, 007 (2019), [arXiv:1802.09216 \[astro-ph.CO\]](#).
 - [38] R. G. Landim, *Eur. Phys. J. C* **79**, 889 (2019), [arXiv:1908.03657 \[gr-qc\]](#).

- [39] E. Di Valentino, A. Melchiorri, and O. Mena, *Phys. Rev. D* **96**, 043503 (2017), [arXiv:1704.08342 \[astro-ph.CO\]](#).
- [40] S. Kumar and R. C. Nunes, *Phys. Rev. D* **96**, 103511 (2017), [arXiv:1702.02143 \[astro-ph.CO\]](#).
- [41] W. Yang, A. Mukherjee, E. Di Valentino, and S. Pan, *Phys. Rev. D* **98**, 123527 (2018), [arXiv:1809.06883 \[astro-ph.CO\]](#).
- [42] W. Yang, S. Pan, E. Di Valentino, R. C. Nunes, S. Vagnozzi, and D. F. Mota, *JCAP* **09**, 019 (2018), [arXiv:1805.08252 \[astro-ph.CO\]](#).
- [43] S. Pan, W. Yang, E. Di Valentino, E. N. Saridakis, and S. Chakraborty, *Phys. Rev. D* **100**, 103520 (2019), [arXiv:1907.07540 \[astro-ph.CO\]](#).
- [44] E. Di Valentino, A. Melchiorri, O. Mena, and S. Vagnozzi, *Phys. Rev. D* **101**, 063502 (2020), [arXiv:1910.09853 \[astro-ph.CO\]](#).
- [45] A. Gómez-Valent, V. Pettorino, and L. Amendola, *Phys. Rev. D* **101**, 123513 (2020), [arXiv:2004.00610 \[astro-ph.CO\]](#).
- [46] J. P. Johnson and S. Shankaranarayanan, *Phys. Rev. D* **103**, 023510 (2021), [arXiv:2006.04618 \[gr-qc\]](#).
- [47] A. Pavlov, S. Westmoreland, K. Saaidi, and B. Ratra, *Phys. Rev. D* **88**, 123513 (2013), [Addendum: *Phys. Rev. D* **88**, 129902 (2013)], [arXiv:1307.7399 \[astro-ph.CO\]](#).
- [48] O. Farooq, F. R. Madiyar, S. Crandall, and B. Ratra, *Astrophys. J.* **835**, 26 (2017), [arXiv:1607.03537 \[astro-ph.CO\]](#).
- [49] J. Simon, L. Verde, and R. Jimenez, *Phys. Rev. D* **71**, 123001 (2005), [arXiv:astro-ph/0412269](#).
- [50] D. Stern, R. Jimenez, L. Verde, S. A. Stanford, and M. Kamionkowski, *Astrophys. J. Suppl.* **188**, 280 (2010), [arXiv:0907.3152 \[astro-ph.CO\]](#).
- [51] M. Moresco *et al.*, *JCAP* **08**, 006 (2012), [arXiv:1201.3609 \[astro-ph.CO\]](#).
- [52] M. Moresco, L. Pozzetti, A. Cimatti, R. Jimenez, C. Maraston, L. Verde, D. Thomas, A. Citro, R. Tojeiro, and D. Wilkinson, *JCAP* **05**, 014 (2016), [arXiv:1601.01701 \[astro-ph.CO\]](#).
- [53] M. Moresco, *Mon. Not. Roy. Astron. Soc.* **450**, L16 (2015), [arXiv:1503.01116 \[astro-ph.CO\]](#).
- [54] C. Zhang, H. Zhang, S. Yuan, T.-J. Zhang, and Y.-C. Sun, *Res. Astron. Astrophys.* **14**, 1221 (2014), [arXiv:1207.4541 \[astro-ph.CO\]](#).
- [55] A. L. Ratsimbazafy, S. I. Loubser, S. M. Crawford, C. M. Cress, B. A. Bassett, R. C. Nichol,

- and P. Väisänen, *Mon. Not. Roy. Astron. Soc.* **467**, 3239 (2017), [arXiv:1702.00418 \[astro-ph.CO\]](#).
- [56] A. L. González-Morán, R. Chávez, R. Terlevich, E. Terlevich, F. Bresolin, D. Fernández-Arenas, M. Plionis, S. Basilakos, J. Melnick, and E. Telles, *Mon. Not. Roy. Astron. Soc.* **487**, 4669 (2019), [arXiv:1906.02195 \[astro-ph.GA\]](#).
 - [57] R. Chávez, R. Terlevich, E. Terlevich, F. Bresolin, J. Melnick, M. Plionis, and S. Basilakos, *Mon. Not. Roy. Astron. Soc.* **442**, 3565 (2014), [arXiv:1405.4010 \[astro-ph.GA\]](#).
 - [58] D. K. Erb, C. C. Steidel, A. E. Shapley, M. Pettini, N. A. Reddy, and K. L. Adelberger, *Astrophys. J.* **646**, 107 (2006), [arXiv:astro-ph/0604041](#).
 - [59] D. Masters *et al.*, *Astrophys. J.* **785**, 153 (2014), [arXiv:1402.0510 \[astro-ph.GA\]](#).
 - [60] M. V. Maseda *et al.*, *Astrophys. J.* **791**, 17 (2014), [arXiv:1406.3351 \[astro-ph.GA\]](#).
 - [61] R. Terlevich, E. Terlevich, J. Melnick, R. Chávez, M. Plionis, F. Bresolin, and S. Basilakos, *Mon. Not. Roy. Astron. Soc.* **451**, 3001 (2015), [arXiv:1505.04376 \[astro-ph.CO\]](#).
 - [62] S. Alam *et al.* (BOSS), *Mon. Not. Roy. Astron. Soc.* **470**, 2617 (2017), [arXiv:1607.03155 \[astro-ph.CO\]](#).
 - [63] F. Beutler, C. Blake, M. Colless, D. H. Jones, L. Staveley-Smith, L. Campbell, Q. Parker, W. Saunders, and F. Watson, *Mon. Not. Roy. Astron. Soc.* **416**, 3017 (2011), [arXiv:1106.3366 \[astro-ph.CO\]](#).
 - [64] A. J. Ross, L. Samushia, C. Howlett, W. J. Percival, A. Burden, and M. Manera, *Mon. Not. Roy. Astron. Soc.* **449**, 835 (2015), [arXiv:1409.3242 \[astro-ph.CO\]](#).
 - [65] M. Ata *et al.*, *Mon. Not. Roy. Astron. Soc.* **473**, 4773 (2018), [arXiv:1705.06373 \[astro-ph.CO\]](#).
 - [66] J. E. Bautista *et al.*, *Astron. Astrophys.* **603**, A12 (2017), [arXiv:1702.00176 \[astro-ph.CO\]](#).
 - [67] A. Font-Ribera *et al.* (BOSS), *JCAP* **05**, 027 (2014), [arXiv:1311.1767 \[astro-ph.CO\]](#).
 - [68] M. Betoule *et al.* (SDSS), *Astron. Astrophys.* **568**, A22 (2014), [arXiv:1401.4064 \[astro-ph.CO\]](#).
 - [69] A. G. Riess *et al.*, *Astrophys. J.* **855**, 136 (2018), [arXiv:1801.01120 \[astro-ph.SR\]](#).
 - [70] A. G. Riess *et al.*, *Astrophys. J.* **826**, 56 (2016), [arXiv:1604.01424 \[astro-ph.CO\]](#).
 - [71] A. G. Riess, S. Casertano, W. Yuan, L. M. Macri, and D. Scolnic, *Astrophys. J.* **876**, 85 (2019), [arXiv:1903.07603 \[astro-ph.CO\]](#).
 - [72] J. Ryan, S. Doshi, and B. Ratra, *Mon. Not. Roy. Astron. Soc.* **480**, 759 (2018), [arXiv:1805.06408 \[astro-ph.CO\]](#).

- [73] J. Ooba, B. Ratra, and N. Sugiyama, *Astrophys. J.* **866**, 68 (2018), [arXiv:1712.08617 \[astro-ph.CO\]](#).
- [74] X.-W. Liu, C. Heneka, and L. Amendola, *JCAP* **05**, 038 (2020), [arXiv:1910.02763 \[astro-ph.CO\]](#).
- [75] M.-J. Zhang and H. Li, (2018), [arXiv:1809.08936 \[astro-ph.CO\]](#).
- [76] A. Sangwan, A. Tripathi, and H. K. Jassal, (2018), [arXiv:1804.09350 \[astro-ph.CO\]](#).
- [77] N. Khadka and B. Ratra, *Mon. Not. Roy. Astron. Soc.* **497**, 263 (2020), [arXiv:2004.09979 \[astro-ph.CO\]](#).
- [78] L. A. Ureña López and N. Roy, *Phys. Rev. D* **102**, 063510 (2020), [arXiv:2007.08873 \[astro-ph.CO\]](#).
- [79] N. Khadka and B. Ratra, *Mon. Not. Roy. Astron. Soc.* **499**, 391 (2020), [arXiv:2007.13907 \[astro-ph.CO\]](#).
- [80] S. Cao, J. Ryan, and B. Ratra, (2021), [arXiv:2101.08817 \[astro-ph.CO\]](#).
- [81] D. Stern, R. Jimenez, L. Verde, M. Kamionkowski, and S. A. Stanford, *JCAP* **2010**, 008 (2010), [arXiv:0907.3149 \[astro-ph.CO\]](#).
- [82] E. Gaztañaga, A. Cabré, and L. Hui, *Mon. Not. Roy. Astron. Soc.* **399**, 1663 (2009), [arXiv:0807.3551 \[astro-ph\]](#).
- [83] M. Sako *et al.* (SDSS), *Publ. Astron. Soc. Pac.* **130**, 064002 (2018), [arXiv:1401.3317 \[astro-ph.CO\]](#).
- [84] A. Conley *et al.* (SNLS), *Astrophys. J. Suppl.* **192**, 1 (2011), [arXiv:1104.1443 \[astro-ph.CO\]](#).
- [85] C. Balland *et al.*, *Astron. Astrophys.* **614**, A134 (2018), [arXiv:1712.07379 \[astro-ph.GA\]](#).
- [86] J. Guy *et al.* (SNLS), *Astron. Astrophys.* **523**, A7 (2010), [arXiv:1010.4743 \[astro-ph.CO\]](#).
- [87] C.-H. Chuang and Y. Wang, *Mon. Not. Roy. Astron. Soc.* **435**, 255 (2013), [arXiv:1209.0210 \[astro-ph.CO\]](#).
- [88] N. G. Busca *et al.*, *Astron. Astrophys.* **552**, A96 (2013), [arXiv:1211.2616 \[astro-ph.CO\]](#).
- [89] C. Blake *et al.*, *Mon. Not. Roy. Astron. Soc.* **425**, 405 (2012), [arXiv:1204.3674 \[astro-ph.CO\]](#).
- [90] E. Aubourg *et al.*, *Phys. Rev. D* **92**, 123516 (2015), [arXiv:1411.1074 \[astro-ph.CO\]](#).
- [91] D. J. Eisenstein *et al.* (SDSS), *Astrophys. J.* **633**, 560 (2005), [arXiv:astro-ph/0501171](#).
- [92] K. D. Gordon, G. C. Clayton, K. A. Misselt, A. U. Landolt, and M. J. Wolff, *The Astrophysical Journal* **594**, 279 (2003), [arXiv:astro-ph/0305257 \[astro-ph\]](#).
- [93] S. Cao, J. Ryan, and B. Ratra, *Mon. Not. Roy. Astron. Soc.* **497**, 3191 (2020),

- arXiv:2005.12617 [astro-ph.CO].
- [94] S. Birrer *et al.*, *Mon. Not. Roy. Astron. Soc.* **484**, 4726 (2019), arXiv:1809.01274 [astro-ph.CO].
 - [95] L. Amendola and Others, *Living Rev. Rel.* **21**, 2 (2018), arXiv:1606.00180 [astro-ph.CO].
 - [96] R. Maartens, F. B. Abdalla, M. Jarvis, and M. G. Santos (SKA Cosmology SWG), *PoS AASKA14*, 016 (2015), arXiv:1501.04076 [astro-ph.CO].
 - [97] M. P. van Haarlem *et al.*, *Astron. Astrophys.* **556**, A2 (2013), arXiv:1305.3550 [astro-ph.IM].
 - [98] H. Hildebrandt *et al.*, *Mon. Not. Roy. Astron. Soc.* **465**, 1454 (2017), arXiv:1606.05338 [astro-ph.CO].
 - [99] A. J. Nishizawa, *PTEP* **2014**, 06B110 (2014), arXiv:1404.5102 [astro-ph.CO].
 - [100] R. G. Crittenden and N. Turok, *Phys. Rev. Lett.* **76**, 575 (1996), arXiv:astro-ph/9510072.
 - [101] J. P. Johnson and S. Shankaranarayanan, *Phys. Rev. D* **100**, 083526 (2019), arXiv:1904.07608 [astro-ph.CO].
 - [102] W. M. Farr, M. Fishbach, J. Ye, and D. Holz, *Astrophys. J. Lett.* **883**, L42 (2019), arXiv:1908.09084 [astro-ph.CO].
 - [103] R. H. Brandenberger, *Rev. Mod. Phys.* **57**, 1 (1985).
 - [104] J. Valiviita, E. Majerotto, and R. Maartens, *JCAP* **07**, 020 (2008), arXiv:0804.0232 [astro-ph].